VIROLOGY

Subnanometer structure of an enveloped virus fusion complex on viral surface reveals new entry mechanisms

Tara C. Marcink[1,2]*, Gillian Zipursky[1,2], Wenjing Cheng[1,2], Kyle Stearns[1,2], Shari Stenglein[1,2], Kate Golub[1,2], Frances Cohen[1,2], Francesca Bovier[1,2], Daniel Pfalmer[3], Alexander L. Greninger[3,4], Matteo Porotto[1,2,5]*, Amedee des Georges[6,7,8]*, Anne Moscona[1,2,9,10]*

Paramyxoviruses—including important pathogens like parainfluenza, measles, and Nipah viruses—use a receptor binding protein [hemagglutinin-neuraminidase (HN) for parainfluenza] and a fusion protein (F), acting in a complex, to enter cells. We use cryo–electron tomography to visualize the fusion complex of human parainfluenza virus 3 (HN/F) on the surface of authentic clinical viruses at a subnanometer resolution sufficient to answer mechanistic questions. An HN loop inserts in a pocket on F, showing how the fusion complex remains in a ready but quiescent state until activation. The globular HN heads are rotated with respect to each other: one downward to contact F, and the other upward to grapple cellular receptors, demonstrating how HN/F performs distinct steps before F activation. This depiction of viral fusion illuminates potentially druggable targets for paramyxoviruses and sheds light on fusion processes that underpin wide-ranging biological processes but have not been visualized in situ or at the present resolution.

INTRODUCTION

Enveloped viruses have evolved surface glycoprotein complexes that mediate fusion of their envelopes with their target cell and deliver the viral genome into the target cell cytoplasm. For the family Paramyxoviridae, which includes a broad swath of human pathogens, this complex consists of two membrane proteins that cooperate to mediate binding and cell entry (*1*). It has become clear that, for all these viruses—whether the receptor binding proteins bind sialic acid moieties, like parainfluenza virus, or proteinaceous receptors, like measles or Nipah viruses—upon receptor engagement, the receptor binding protein triggers the fusion protein to activate fusion and viral entry.

For human parainfluenza virus 3 (HPIV3), the fusion/entry apparatus consists of the receptor binding protein hemagglutinin-neuraminidase (HN) in complex with the fusion protein (F). The series of cooperative steps that mediate entry have been elucidated since it was first demonstrated, using HPIV3 as the prototype, which for most Paramyxoviridae virus–induced membrane fusion requires active participation of both HN (or H or G, depending on the virus) and F (*2*–*7*). F is synthesized as a metastable proprotein in its prefusion state (*8*–*10*). HN stabilizes the F protein before receptor is engaged to prevent viral inactivation (*5*). Once host cell receptors have been engaged, HN switches to new roles: The HN stalk communicates with two sites in the HN head, thereby activating the trimeric fusion (F) protein, inducing a conformational change in F that allows for its insertion into the host cell membrane (*3*, *8*, *11*–*13*). F extends to insert into the target cell membrane and refolds to mediate virus-cell fusion and viral entry (*3*, *4*, *6*, *11*, *14*). A notable challenge to understanding these processes has been the lack of structural information about the intact receptor binding protein—fusion protein complex present in the viral membrane surface of authentic viruses. The structures of the HN/F complex of circulating HPIV3 [clinical isolates (CIs)] in situ on the viral surface membrane before receptor engagement, presented here, begin to reveal exactly how these two molecules carry out this precise program in sequence.

Structures of the soluble portion of individual paramyxovirus HN (or H or G) and F proteins have provided clues to the function of this HN/F fusion complex and led to conflicting models for the mechanism of action of the paramyxovirus fusion complex during entry (*8*, *15*–*18*), but the models agree that HN, upon receptor engagement, triggers the metastable, prefusion F to undergo the series of structural transitions that result in fusion of the viral and cellular membranes (*1*). Crystal structures of the soluble domains of receptor binding proteins are available for measles H; Nipah virus, Hendra virus, and respiratory syncytial virus G; and HPIV3, HPIV1, PIV5, and Newcastle disease virus (NDV) HNs and for the same viruses' fusion (F) proteins (*6*, *19*–*24*). The type II receptor binding membrane proteins (HN for HPIV3) contain an N-terminal cytoplasmic domain, a membrane-spanning region, a stalk region, and a globular head. The four activities of HPIV3 HN—stabilization of prefusion F, receptor binding, F triggering, and receptor cleaving—are regulated precisely depending on the stage of viral entry or egress. The stalk confers specificity for the homologous F in the fusion activation process (*3*, *11*, *25*–*28*). HN's primary binding site, which has both receptor binding and receptor cleaving (neuraminidase) activities (primary sialic acid-binding site I; "site I"), is

[1]Department of Pediatrics, Columbia University Vagelos College of Physicians and Surgeons, New York, NY, USA. [2]Center for Host-Pathogen Interaction, Columbia University Vagelos College of Physicians and Surgeons, New York, NY, USA. [3]Department of Laboratory Medicine and Pathology, University of Washington, Seattle, WA, USA. [4]Vaccine and Infectious Disease Division, Fred Hutchinson Cancer Research Center, Seattle, WA, USA. [5]Department of Experimental Medicine, University of Campania "Luigi Vanvitelli," 81100 Caserta, Italy. [6]Structural Biology Initiative, CUNY Advanced Science Research Center, City University of New York, New York, NY, USA. [7]Department of Chemistry and Biochemistry, The City College of New York, New York, NY, USA. [8]PhD Programs in Chemistry and Biochemistry, The Graduate Center, City University of New York, New York, NY, USA. [9]Department of Microbiology and Immunology, Columbia University Vagelos College of Physicians and Surgeons, New York, NY, USA. [10]Department of Physiology and Cellular Biophysics, Columbia University Vagelos College of Physicians and Surgeons, New York, NY, USA.
*Corresponding author. Email: tm2996@cumc.columbia.edu (T.C.M.); mp3509@cumc.columbia.edu (M.P.); adesgeorges@gc.cuny.edu (A.d.G.); am939@cumc.columbia.edu (A.M.)

located on the globular head for HPIV3 (and other paramyxoviruses for which structural information is available) (*17*, *19*, *29*).

The type I transmembrane F proteins are trimers with shorter stalks than those of HN and large globular heads (*10*, *30*). While the HPIV F protein is dissimilar in structure to other class I viral fusion proteins, it shares with others—including severe acute respiratory syndrome coronavirus disease 2 spike (S) (*31*), Ebola virus glycoprotein (GP) (*32*), influenza hemagglutinin (HA) (*33*), and HIV Env (*34*)—the strategy for membrane fusion, which entails reorientation from a small prefusion state to an extended intermediate state after activation. In the prefusion state, the F is in a metastable prefusion conformation and, for all fusion-entering viruses, must be maintained in this preactive state by some means. The structure of HPIV3 prefusion F was solved by cryo–electron microscopy (cryo-EM) with the aid of mutations that stabilize the prefusion state and complexed with a prefusion-specific neutralizing antibody (PIA174 Ab) that binds the apex of the prefusion F trimer at antigenic site Ø (*10*, *35*). These structures of soluble domains provide information on the general structure of individual glycoproteins, although do not indicate how these glycoproteins interact in a complex on the viral surface.

The HN/F complex first retains F in its prefusion state and then, only upon receptor engagement, responds by effecting major structural transitions. We previously showed that, on viral surfaces, HN and F were colocalized before receptor engagement (*14*). Cryo–electron tomography (cryo-ET) showed that HN was present in a canopy over the prefusion F in close association with F (*1*, *7*). In virions that were examined without disruptive purification steps, this HN canopy extends across the entirety of the virus′ surface, closely associated with prefusion F in the absence of target cell receptors and resting above F in what appears to be a possible mechanism for protecting F from activation (*7*). The mechanism by which HN protects F from activation and triggers its release upon receptor binding is unknown. To investigate these mechanisms key to virus entry into the host, we used cryo-ET to obtain the subnanometer resolution of the HN/F complexes of CIs of HPIV3 on the virus′ surface. These human viruses bear HN/F fusion complexes that are suited to the natural environment and differ significantly in function from viruses that have been used until recently for biological or structural studies (*12*, *13*). The structure reveals the molecular details of the interaction between prefusion F and HN globular heads as well as a novel conformation of HN dimeric heads.

At the resolution that we obtained, HN is present as a dimer on the intact virus surface and is not a tetramer (or dimer of dimers) as has been proposed for other paramyxoviruses (*7*). One of the globular heads of the HN dimer caps the apex of prefusion F and extends a loop downward to contact a pocket within F, at a site overlapping the epitope of the prefusion specific fusion-neutralizing monoclonal antibody PIA174. This F-engaged HN loop structure is highly conserved across paramyxoviruses and may be a general mechanism for maintaining the fusion/entry complex′s stability and ensuring that activation of fusion occurs only at the right time and location. The other HN globular head in the dimer, distal to F, is positioned with site I exposed above the complex, pointing upward toward a putative receptor. This suggests that, in each HN dimer, the heads are arranged asymmetrically, with one protomer′s binding site available to bind the sialic acid receptor, while the other protomer interacts with and stabilizes the prefusion form of F. The structure reported here suggests the potential for rotational flexibility between the protomeric heads of HN around the HN dimer interface that, together with mutational data about the HN dimer interface, intimates a previously unknown step in activation of F. This structure of an authentic preactivation HN/F complex reveals an unexpected organization of the glycoproteins and essential interactions between HN and F in the prefusion state of the entry complex on the viral surface and suggests general principles for fusion complexes that need to pack several distinct essential functions into one or two viral surface proteins.

RESULTS

Subnanometer resolution of HPIV3 fusion/entry complex on the surface of clinical isolate virions

Circulating HPIV3 viruses that cause human disease bear HN/F fusion complexes that differ significantly from the complexes from laboratory-adapted strains previously used to study function and structure. The HPIV3 CIs have HN/F pairs that are poorly suited to infect cultured cells, and culture-adaptive mutations occur that alter the behavior of these complexes (*6*, *12*, *13*, *36*, *37*). In particular, the dimer interface between the HN globular heads is key in modulating fusion activation and is prone to evolve under the selective pressure of distinct infection environments (*6*, *12*, *13*, *36*). To correlate structure with function of the authentic entry apparatus, we use CI viruses captured directly from human airway epithelial tissue culture, or engineered viruses based on the CI genome, for cryo-ET structural study of authentic HN/F complexes. The viruses captured directly on grids without high-speed centrifugation or other disruptive steps bear intact lipid bilayers and complexes composed of prefusion F adjacent to and below HN molecules, with the globular heads of the HN protomers positioned above F (Fig. 1A) (*7*).

HN and F cover the entire intact viral surface (Fig. 1A) and were used for subtomogram averaging; final subtomogram averages included only those HN and F pairs from multiple viruses with the highest cross correlation (i.e., best fit) compared to the reference structure (Fig. 1, B to I; figs. S1 to S3; and movies S1 and S2). To maximize the resolution of our subtomogram averages, we used a tailored processing pipeline that includes adaptation of single-particle strategies [Warp/M; (*38*)] that optimize frame and tilt alignment parameters at the level of each particle, so that we generated subtomograms from particles extracted directly from the tilt series rather than from the full tomograms (fig. S2 and the materials and methods section) and obtained subtomogram averages of the HN/F complex at an overall resolution of 10.2 Å. Further refinement that focused on the HN or F globular heads yielded subtomogram averages at resolutions of 8.5 and 9.3 Å, respectively (Fig. 1, C to G; and fig. S3, A to E). The model derived from the cryo-EM structure of the soluble portion of F [Protein Data Bank (PDB) ID: 6MJZ; (*10*)] was fit into the final density (Fig. 1, F to G, and movie S2). The model of individual HN protomer heads, which were derived from the crystal structure of the soluble portion of the HN dimer [PDB ID: 4MZA; (*6*)], was also fit into the final density with a model-to-map Fourier shell correlation (FSC) of 9.0 Å (Fig. 1, F and G; fig. S3, F to I; and movie S2). The fit-to-map cross-correlation values were better for the individually fit HN globular head protomers (0.86) (fig. S3H) than for the crystal structure of the soluble HN dimeric globular heads (0.82) (fig. S3G) and showed

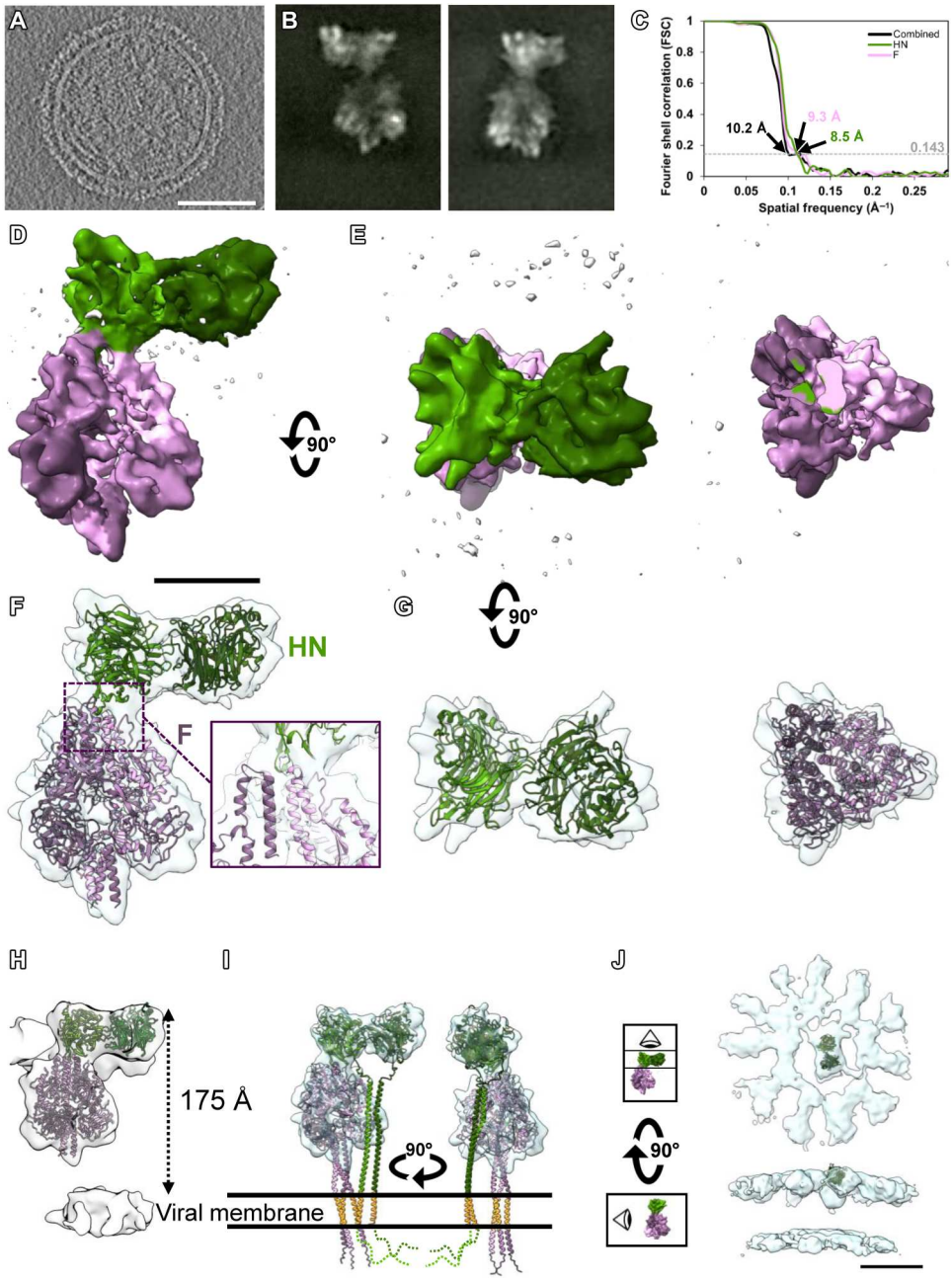

Fig. 1. Subnanometer resolution of the HN/F viral fusion complex on the virus surface. (**A**) Representative central slice from a tomogram of an HPIV3 viral particle. (**B**) *X* and *Y* projections from final subtomogram complex reconstruction using a tight mask around HN and F. (**C**) Fourier shell correlation (FSC) plots of the HN and F complex with and without a mask and the individual HN- and F-focused refinements. Side views and top view of the final HN (green) and F (pink) reconstruction without (**D** and **E**) and with (**F** and **G**) prefusion F [Protein Data Bank (PDB) ID: 6MJZ] and HN (PDB ID: 4MZA) models fit into the density. Side view of the prefusion F apex region with clear α-helical densities is shown in the inset. (G) HN and F each separately in top-down view with the models fit into the density. (**H**) Side view of the HN/F complex reconstruction filtered to 20 Å and with prefusion F (PDB ID: 6MJZ) and HN (PDB ID: 4MZA) models fit into the density. The density threshold level was decreased to reveal the viral membrane. (**I**) Full-length HN (green model) and F (pink model) derived from a combination of the soluble F structure (PDB ID: 6MJZ) and the AlphaFold model of the F trimer stalk region were fit into our final subvolumes. (**J**) Subtomogram-averaged volume of the glycoprotein organization on the viral surface (one of the five classes from a particle classification is shown, revealing separated dimers; see also fig. S1 for additional classes). Scale bars, (A) 50 nm, (D) 5 nm, and (J) 10 nm.

better fit in the density. The HN dimer heads extend 175 Å above the viral membrane surface, above F (Fig. 1, H and I). We do not observe the long α-helical HN stalk, most likely due to its flexibility. Therefore, we modeled an extended HN dimer derived from AlphaFold structure prediction software (*39*, *40*) and fit this model into our final subvolume, supporting the notion that the subtomograms are compatible with the complex inserted into the viral membrane (Fig. 1I).

At the final resolution, the head of one of the two HN protomers is observed to interact with the apex of F (Fig. 1F). The side view (Fig. 1F) reveals the orientation of HN in relation to F. One globular head interacts with F, while the other is positioned distal to F and does not interact with F. F′s structure is consistent with the previously solved cryo-EM structure of soluble prefusion F (*10*). α Helices, while not completely resolved, can be seen in the stalk of F in the density map and in the apex of F (fig. S3I); fig. S3I (far right panel) shows the stalk separately as if viewed from above, where the α helix resolution can be better observed. The F apex appears rigid, as suggested by the high local resolution (fig. S3I). Of note, much of the stalk region of F is resolved in this complex without the need for stabilizing mutations to retain F in its prefusion state as was required for the soluble fusion proteins of related viruses (*10*, *41*–*43*).

The densities that we observe on the intact virus surface are consistent with HN forming a dimer, when resolved in its complex with F (fig. S3H). We do not find evidence for a tetramer or dimer of dimers. To better capture the ultrastructure of the HN canopy, we performed subtomogram averaging and classification of a larger area on the viral surface using a mask encompassing only the HN canopy. Density maps from this classification (Fig. 1J and fig. S1C) show the level of variability of the HN canopy and lack of defined ultrastructure beyond the HN dimer. This view of the HN canopy further supports that HN is present at the viral surface as dimers that are separated from each other and does not show tetrameric-like densities or evidence of stable interactions beyond the dimer.

Relationship between HN globular heads in the complex

In the HN/F complex, we observe that, in each HN dimer, the heads are rotated with respect to each other, with one protomer′s binding site well positioned to bind the sialic acid receptor, while the other protomer is rotated to interact with and stabilize the prefusion form of F. The globular head of one HN protomer—the protomer distal to F—is positioned with its primary sialic acid–binding site (*19*) exposed above the complex and pointing upward, in the direction of a putative receptor (Fig. 2, A and E). The globular head of the HN protomer proximal to F is rotated with respect to the other protomer′s head (Fig. 2, A, C, and E), so that its primary sialic acid–binding site near the protomer′s center of mass (Fig. 2E, red sphere) is facing orthogonally in relation to the viral membrane in Fig. 2A. This suggests an organization where, in each HN dimer, one protomer interacts with F, while the other is available to bind the sialic acid receptor.

For the cryo-ET model, when the HN protomer head structures are individually fit into the cryo-ET density as in Fig. 2A, the fit and the axis of rotation (*Z*′) between the protomers is consistent with the angle of the HN/F complex with respect to the viral membrane (90° in the *z* direction, tilt of 5°) and fits into the density (Fig. 2C and fig. S3H). However, if the dimeric head crystal structure complex is aligned to the cryo-ET model proximal to F as in Fig. 2B, then the fit and the axis of rotation (*Z*′) yields a tilt of 25° with respect to an axis perpendicular to the viral membrane (Fig. 2B) and the HN protomer distal to F does not fit into the density (Fig. 2D). In the cryo-ET model, when looking down the *Z*′ axis of rotation (Fig. 2E, purple bar), there is an angle of 156° between the two HN protomers′ heads with respect to the *Z*′ axis. In contrast, in the crystal structure model, this angle is 178° (Fig. 2F).

The smaller angle between the protomer heads with respect to the *Z*′ axis in the cryo-ET structure compared to the crystal structure results in a reduced number of residues (the buried surface area) interacting with the opposing protomer at the dimer interface (Fig. 2, G and H) and a longer distance between the centers of mass of each protomer head (51 Å; Fig. 2E, red spheres) compared to the crystal model (43 Å; Fig. 2F). The heads are in a more relaxed configuration in the cryo-ET model, which we refer to as the "loose" configuration, compared to the "tight" configuration suggested by the crystal structure. A similar difference in HN dimer configuration has been observed for NDV (*17*) with different crystallization conditions; the low-pH structure shows a loose configuration [PDB ID: 1E8U; (*17*)], while the high-pH configuration shows tight interaction between the heads [PDB ID: 1E8V; (*17*)] (fig. S4). Molecular dynamic studies supported the notion that the HN heads can assume these different conformations and rotate with respect to each other (*44*).

The HN dimer interface is important for HN′s role in activating F and is a key to transmission of the signal for fusion upon receptor engagement (*11*–*14*, *36*). In the crystal structure of the soluble HPIV3 HN dimer, the heads of the protomers are in tight contact at the secondary binding site that forms at the dimer interface and that we have shown to play a role in activating F (*6*, *19*, *45*). We previously showed crystallographically that a mutation in the globular head of HN (Q559R, a residue adjacent to the dimer interface but not contacting the opposing protomer in the dimer interface) relaxes the HN dimer interface in the crystal structure, with a reduced number of residues interacting with the opposing protomer at the dimer interface, and showed that this mutation decreases HN/F interaction (*6*). This mutation also decreases fusion activation (*6*, *11*–*13*, *36*). Several other dimer-interface mutations in HN [HN N551D and HN H552Q; (*11*)] decrease HN′s capacity for stabilizing prefusion F and also enhance HN′s activation of F. These residues are within the HN dimer interface in both the crystal structure and the cryo-ET structure (Fig. 2, G and H). The dimer interface region near residue H552, a residue that we know to be critical for receptor binding and F activation (*11*–*14*), closely resembles the crystal structure (Fig. 2, G and H) and is the region of the interface with least divergence between the soluble crystal structure and our subtomogram average in the complex (Fig. 2, G and H). The difference in the angle between the protomer heads in the cryo-ET conformation and the crystal conformation, which alters the residues interacting with the opposing protomer at the dimer interface, raises the possibility that there is freedom of movement between the HN protomer heads.

Relationship between HN and F in the complex

The globular head of the HN protomer directly above F, positioned as shown in the full-length cryo-ET AlphaFold-derived model of HN + F fit into the cryo-ET density (Fig. 3A), contains a loop composed of residues 386 to 392 that extends downward to engage with residues 188 to 196 at the apex of the F trimer. In Fig. 3B, this

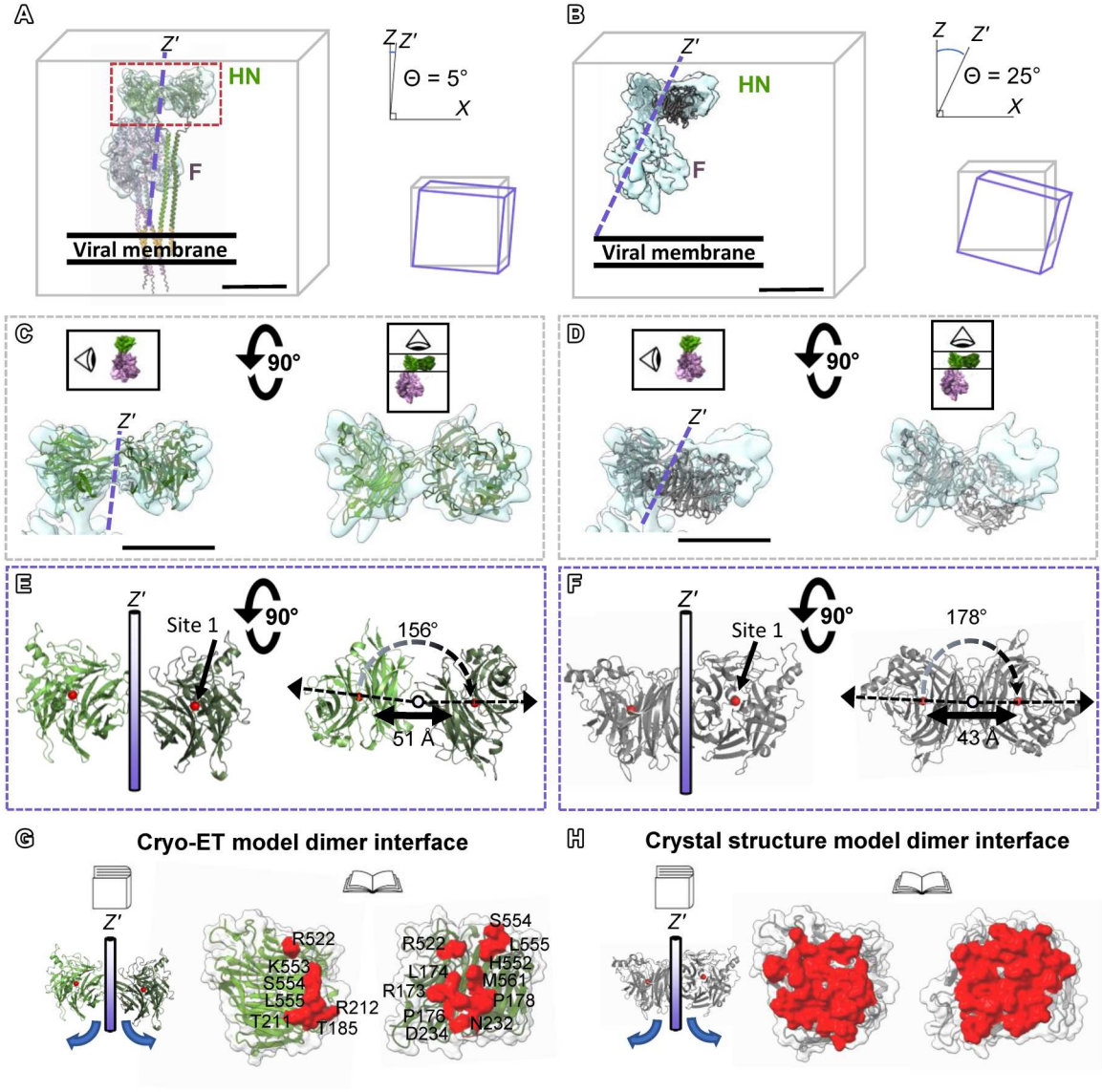

Fig. 2. Interactions between HN protomer heads observed in cryo-ET reconstructions compared with the crystal structure of soluble HN dimer. (**A**) Full-length cryo-ET AlphaFold model of HN + F. Dashed box: HN protomers individually fit into cryo-ET density. (**B**) Crystal structure model of dimeric HN (PDB ID: 4MZA) fit into cryo-ET density. Axis of rotation around HN (*Z*′; purple dashed lines) plotted in relation to viral membrane. When compared to the *z* axis of viral membrane (gray cube), axis of rotation around HN is tilted 5° for the cryo-ET model (A) and 25° for the crystal structure model (B) (purple cubes). (**C**) Zoomed-in side, top views of individual HN protomer heads from crystal structure (green) fit into cryo-ET density. (**D**) Zoomed-in side, top views of HN dimer heads from crystal structure (gray) placed into cryo-ET density by fitting only proximal HN protomer head. (**E**) Cryo-ET model has 156° between HN protomer heads with respect to the *Z*′ axis (purple bar) and 51 Å between the HN protomer centers (red spheres). (**F**) Crystal structure model has 178° between the two HN protomers' heads with respect to the *Z*′ axis (purple bar) and 43 Å between the centers. (**G** and **H**) Peeling opens the HN dimer for each model so that the interfaces face out. Surfaces that contact the opposing protomer in the cryo-ET model are red (G). Buried surface area in the cryo-ET structure (red) is less than the buried surface area in the crystal structure (H). Scale bars (A to D), 5 nm.

interaction is placed into the cryo-ET density, and in Fig. 3C, the corresponding cartoon is shown. This 386 to 392 HN loop nestles in the space formed between the protomers of the F trimer, occupying a hydrophobic pocket at the F apex (Fig. 3D). The interaction creates a "thumb-finger" motif in HN facing the F apex, where the "thumb" is the 386 to 392 HN loop, and the "finger" is a β sheet and second loop comprising HN residues 294 to 300 (Fig. 3, B and C). Within the HN loop, residues K386, L388, S390, and V391 appear to contact residues in F (Fig. 3E). Additional density observed at the location of glycosylated residue N308 of HN is tentatively attributed to the sugar and extends toward F, suggesting that the sugar may also interact with the apex of F (Fig. 3F). Figure 3G shows schematically how the HN protomer appears to cap F with these three contact points.

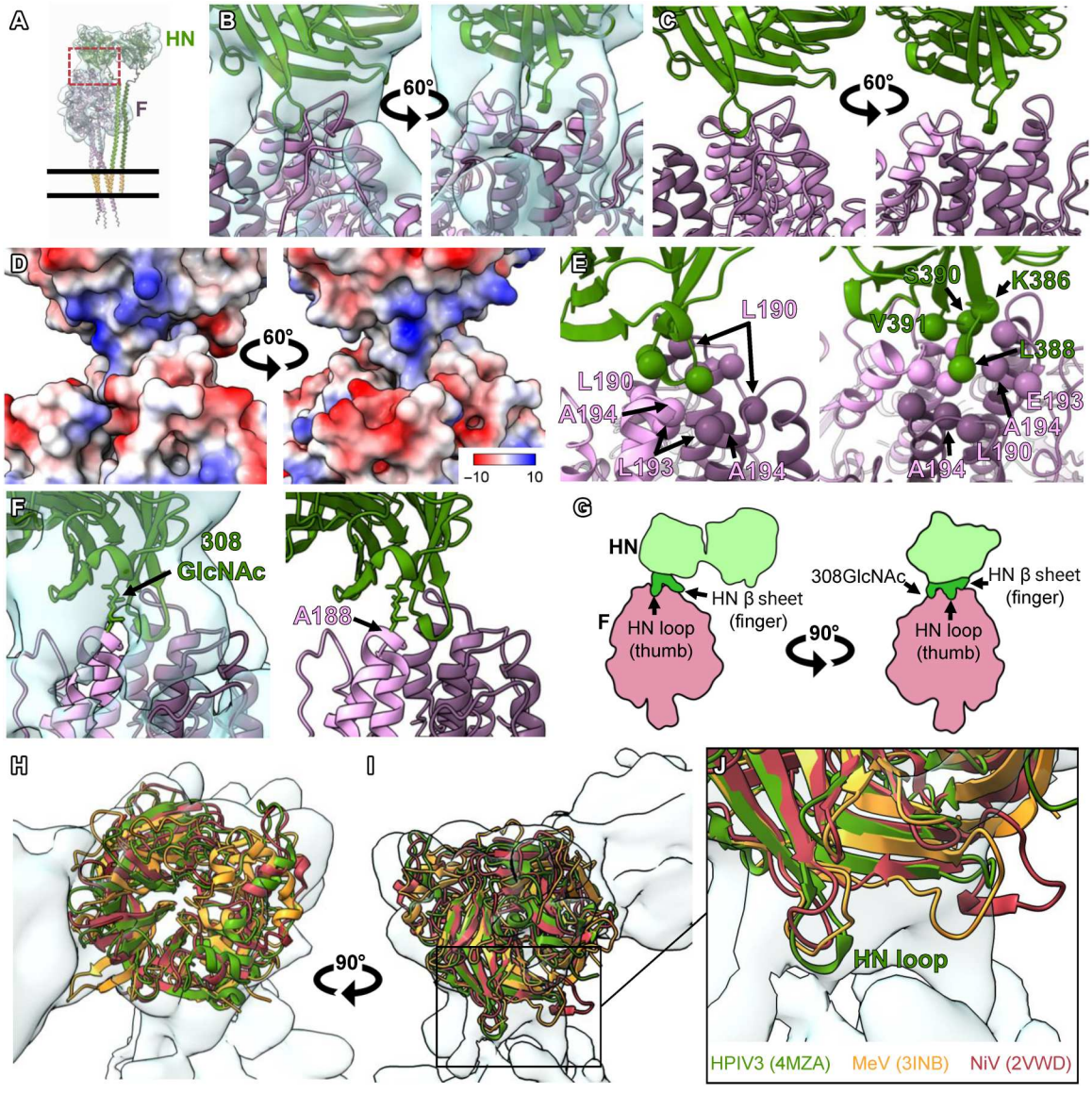

Fig. 3. Loop motif of the HN protomeric head interacting with the apex of F. (**A**) Full-length cryo-ET AlphaFold-derived model of HN + F fit into the cryo-ET density. The dashed box indicates the HN/F interaction region under discussion. (**B**) Zoomed-in view of the final reconstruction focused on the HN/F interaction. (**C**) Models of HN (green) and F (pink) fit into the density of (A) with the HN loop interacting with the apex of F. (**D**) Electrostatic potential of the HN/F interaction region under discussion. (**E**) Individual residues of HN and F (spheres) that are in close interaction with each other at the F apex. (**F**) Density corresponding to an N-linked glycosylation site that is involved with the HN/F interaction region. The model has one hydrogen bond between the apex of F and the sugar molecule on HN . (**G**) Schematic side views of the thumb-finger motif that appears to position the HN protomer above F. (**H** to **J**) Overlay of measles H (yellow) and Nipah G (red) on the HPIV3 HN protomer (green) with comparison showing the similarities in receptor binding site 1 (H) along with the thumb finger motif (I and J).

Parallel relationship between the receptor binding and fusion protein in other paramyxoviruses

The related paramyxoviruses measles virus and Nipah virus have a HA (H) and G protein, respectively, as receptor binding proteins, and there is no sequence conservation in this domain of the receptor binding proteins. However, overlay of the HPIV3 HN globular heads density with those of measles virus H and Nipah virus G shows notable conservation of structure in this thumb-finger motif (Fig. 3, H to J). Despite marked variability in the amino acid sequences of these loops among these viruses (which also includes Hendra virus G, NDV HN, and PIV5 HN; fig. S5A), the overlay of each structure points to the structural conservation of this loop and of its relationship to F (fig. S5B).

Prefusion F Fab antibody and HN bind the same region at the apex of F

An anti–F-neutralizing antibody that inhibits infection (PIA174) binds to the apex of F at the same site as HN in the HN/F complex (*10*). The structure of the HPIV3-neutralizing Fab antibody (PIA174) complexed with the stabilized soluble region of prefusion F was solved by cryo-EM (*10*). The Fab fragment bound to the apex of F at antigenic site Ø (Fig. 4A). The site on F bound by the

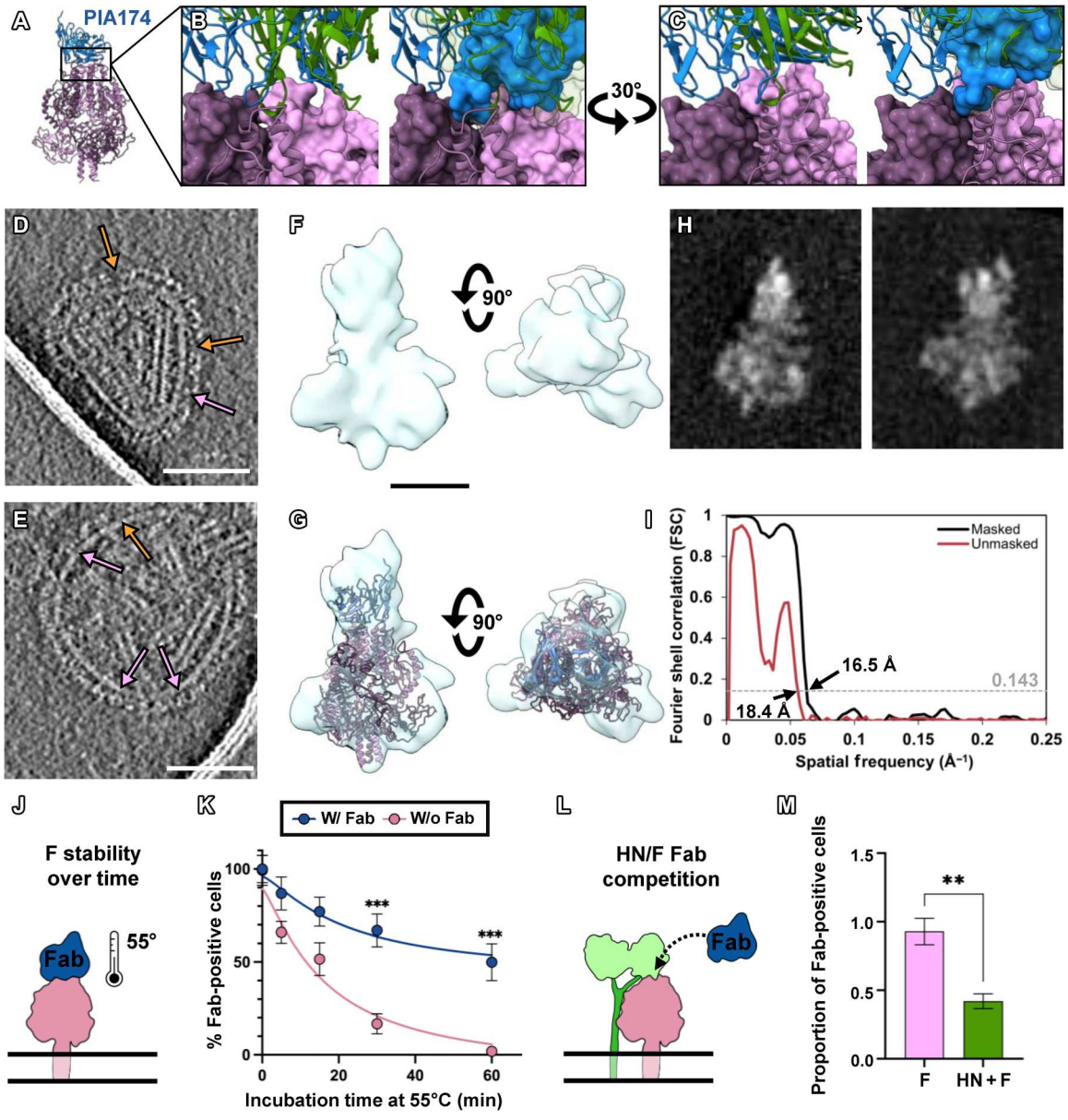

Fig. 4. Anti–F-neutralizing antibody and HN both bind at the apex of prefusion F. (**A**) Cryo-EM structure of soluble prefusion F (pink) bound to anti–F-neutralizing PIA174 Fab (blue) (PDB ID: 6MJZ). (**B** and **C**) Overlay of PIA174 Fab surface (blue) with (B) and without (C) the surface from the cryo-ET model with Fab (blue), HN (green), and F (pink). (**D** and **E**) Disruption of viral surface by PIA174 Fab showing regions of viral surface with no density (orange arrows) or F only without HN (pink arrows). (**F** and **G**) Subtomogram average without (F) and with (G) the fit of the PIA174 Fab cryo-EM structure. (**H**) *X* and *Y* projection slices from subtomogram reconstruction of selected particles on the viral surface containing PIA174 bound to prefusion F. (**I**) Plots of FSCs from the final subvolume of the PIA174 Fab bound to F complex with masked and unmasked resolution at the 0.143-Å cutoff value. (**J** and **K**) Schematic (J) of assay for PIA174 Fab stabilization of prefusion F (heat temperature–mediated activation of F at 55°C) in the absence of HN. (K) Percent cells with prefusion F after varying incubation durations at 55°C with prefusion-specific PIA174 Fab, normalized to F alone and incubated with Fab at 4°C. ***$P \leq 0.001$ by two-way analysis of variance (ANOVA) and Sidak's post hoc test. (**L**) Schematic of competition between HN and PIA174. (**M**) Proportion of PIA174 Fab binding to cells expressing F alone (pink bar) or F + HN (green bar) in presence versus absence of DTSSP. Data are means ± SE from three separate experiments. **$P \leq 0.01$ by unpaired two-tailed *t* test. Scale bars, (D and E) 50 and (F) 10 nm.

PIA174 Fab in this structure precisely overlaps the domain bound by the 386 to 392 HN loop (Fig. 4, B to C, and movie S3). Unexpectedly, the Fab antibody fragment contains a very similar thumb-finger motif facing the apex of F as observed in the HN loop, evident in the overlay of the neutralizing Fab antibody atomic surface with the cryo-ET model of HN and F (Fig. 4, A to C).

To assess functional overlap between the sites bound by HN and the neutralizing Fab, we added the PIA174 Fab to viruses before vitrification and imaged the resulting sample by cryo-ET. The surface organization of HN and F was altered by the PIA174 Fab with missing surface glycoprotein densities (Fig. 4, D and E, orange arrows) and evidence of F glycoprotein present alone (Fig. 4, D

and E, pink arrows), suggesting a disruption of the HN/F complex (Fig. 4, D and E, and fig. S6). Subtomogram averaging of the viral surface on a subset of particles from six of these tomograms reveals prefusion F bound to PIA174 Fab at a 16-Å resolution (Fig. 4, F to I, and figs. S2B and S6). The published soluble cryo-EM structure of PIA174-F complex (PDB ID: 6MJZ) (*10*) fits closely into our subtomogram average density (Fig. 4, F and G; fig. S6C; and movie S4).

To determine whether the PIA174 Fab stabilizes prefusion F and prevents heat temperature–mediated activation of F at 55°C in the absence of HN (*5*) (schematic in Fig. 4J), cells expressing F in the presence or absence of the PIA174 Fab were incubated at 55°C for varying times. Without PIA174, the proportion of F in its prefusion state rapidly decreases, as all the prefusion F is activated by temperature (Fig. 4K, pink line). However, in the presence of PIA174 added before the onset of heat, F maintains its prefusion state (Fig. 4K, blue line). This observation that PIA174 stabilizes the prefusion F holds when the same experiment is performed with a conformation-specific Ab that recognizes postfusion F (monoclonal antibody PA3/F4) (fig. S7) (*46*).

To obtain functional evidence for an overlapping binding domain on prefusion F for HN and PIA174 Fab, we determined whether HN can mask the epitope of the PIA174 Fab binding site in HN/F complexes on the cell surface (schematic in Fig. 4L). Cells expressing F alone or HN/F were either pretreated or not treated with the cross-linker 3,3'-Dithiobis(sulfosuccinimidyl propionate (DTSSP) and then incubated with PIA174 Fab. PIA174 Fab binding was quantitated (Fig. 4M, bars show proportion of Fab binding after compared to before cross-linking). Fab antibody binding to prefusion F was similar in the absence or presence of DTSSP, as expected (pink bar). However, Fab antibody binding to DTSSP-pretreated prefusion F and HN was decreased, suggesting that HN cross-linked with F masks the PIA174 Fab antibody binding site (green bar).

Alterations at key HN/F interface probed with neutralizing anti-F antibody

To examine the functional consequences of the overlapping binding epitopes of HN and PIA174 on F, we used specific mutations derived from both structural and functional information. We conducted a viral evolution experiment using the selective pressure of growth of virus in the presence of increasing concentrations of Ab PIA174. Two particularly salient mutations arose in Ab escape variant (fig. S8); F-A194T at the F apex at the interface between F and Ab PIA174 and HN-H552Q at the HN dimer interface with enhanced F activation properties (*6*, *11*, *13*, *14*). The resulting virus was no longer neutralized by Ab PIA174 even at the highest concentrations (Fig. 5A). In expressed F, the A194T mutation decreases PIA174 antibody binding (Fig. 5B). In silico modeling of the F-A194T in the soluble cryo-EM structure shows that the bulkier threonine (T) residue in this pocket may produce steric clash with the Ab loop at this site (Fig. 5, C to E). To evaluate the effect of A194T on Ab-mediated inhibition of fusion, we measured inhibition of F-mediated fusion by PIA174 Ab in a quantitative cell-cell fusion assay using (*11*) cells coexpressing F (parental and A194T) and HN (parental) or influenza HA, which provides membrane tethering via sialic acid receptor engagement but does not complex with, or activate, F (Fig. 5, F and G) (*5*, *14*). The parental F, when paired with either HN (green triangles) or HA (red triangles) was inhibited by PIA174 Ab. The F-A194T when paired with either HN (orange circles) or HA (purple circles) was resistant to inhibition by the PIA174 Ab (Fig. 5H). The resistance to PIA174 Ab inhibition of A194T F-mediated fusion (Fig. 5H) is less than the resistance to the PIA174 Fab demonstrated by the escape variant virus bearing the full complement of four escape mutations in HN and F (see fig. S8).

We evaluated the impact of the A194T mutation in F on the ability of F to be activated by heat or by HN, using an assay that distinguishes between different states of F activation (*11*, *47*). The readout for F activation is fusion of red blood cells (RBCs) with the F-expressing cells. Cells coexpressing F and HN or HA were allowed to bind to their sialic acid receptors on RBCs at 4°C and transferred to a range of temperatures to permit F activation. At each temperature, we measured the percentage of target RBCs that were either released into the medium (blue circles), bound but had not fused, indicating that they were either bound by HN/HA (red square) or had undergone fusion (green triangle). The F A194T is more readily triggered by heat compared to the parental F (Fig. 5, I and J; compare 50% fusion temperature for HA + F A194T indicated by orange dotted line to 50% fusion temperature for HA + parental F indicated by pink solid line). The F A194T is less readily activated in the presence of HN (Fig. 5, K and L; compare 50% fusion temperature for HN+ F A194T indicated by orange dashed line to 50% fusion temperature for HN + parental F indicated by pink dashed line), suggesting that the HN/F interaction has been perturbed. The findings that viral evolution under selective pressure of PIA174 Ab led to a mutation at the precise site that we predict to be the site of HN/F interaction and that this mutation alters both PIA174 Ab binding and HN′s activation of F support the notion that this HN/F interaction site represents an important interface between HN and F and functionally overlaps with the site of PIA174-neutralizing antibody binding. Together, the results in Figs. 4 and 5 suggest that the neutralizing Ab PIA174 inhibits fusion by stabilizing the prefusion state of F and competing with HN and thereby inhibiting F activation.

DISCUSSION

The family Paramyxoviridae includes important pathogens like parainfluenza virus, measles virus, and Nipah virus, all of which use a receptor binding protein and fusion protein, acting in concert in a complex, to enter cells. In the general principle that has emerged for this family of viruses, upon receptor engagement, the receptor binding protein activates the fusion protein, triggering membrane merger and entry. This general mechanism is true whether the specific receptor binding proteins engage sialic acid moieties, like parainfluenza, or proteinaceous receptors, like measles or Nipah viruses. The paramyxovirus fusion machinery (HN/H/G and F) has been studied in cell biological assays (*4*, *11*, *47*, *48*) or biochemical settings (*5*, *6*, *14*, *49*, *50*) but never as a functional complex on authentic virions. Very few high-resolution (<10-Å) surface glycoprotein structures of enveloped viral glycoproteins have been solved (*51*–*55*), and no structures of asymmetric viral fusion complexes in situ have previously been solved by subtomographic averaging at high resolution. Key questions about the mechanism of this complex could not be answered without high-resolution structural information. To understand how the two proteins of the fusion complex work together in a molecular machine to accomplish entry, we designed approaches to study the intact

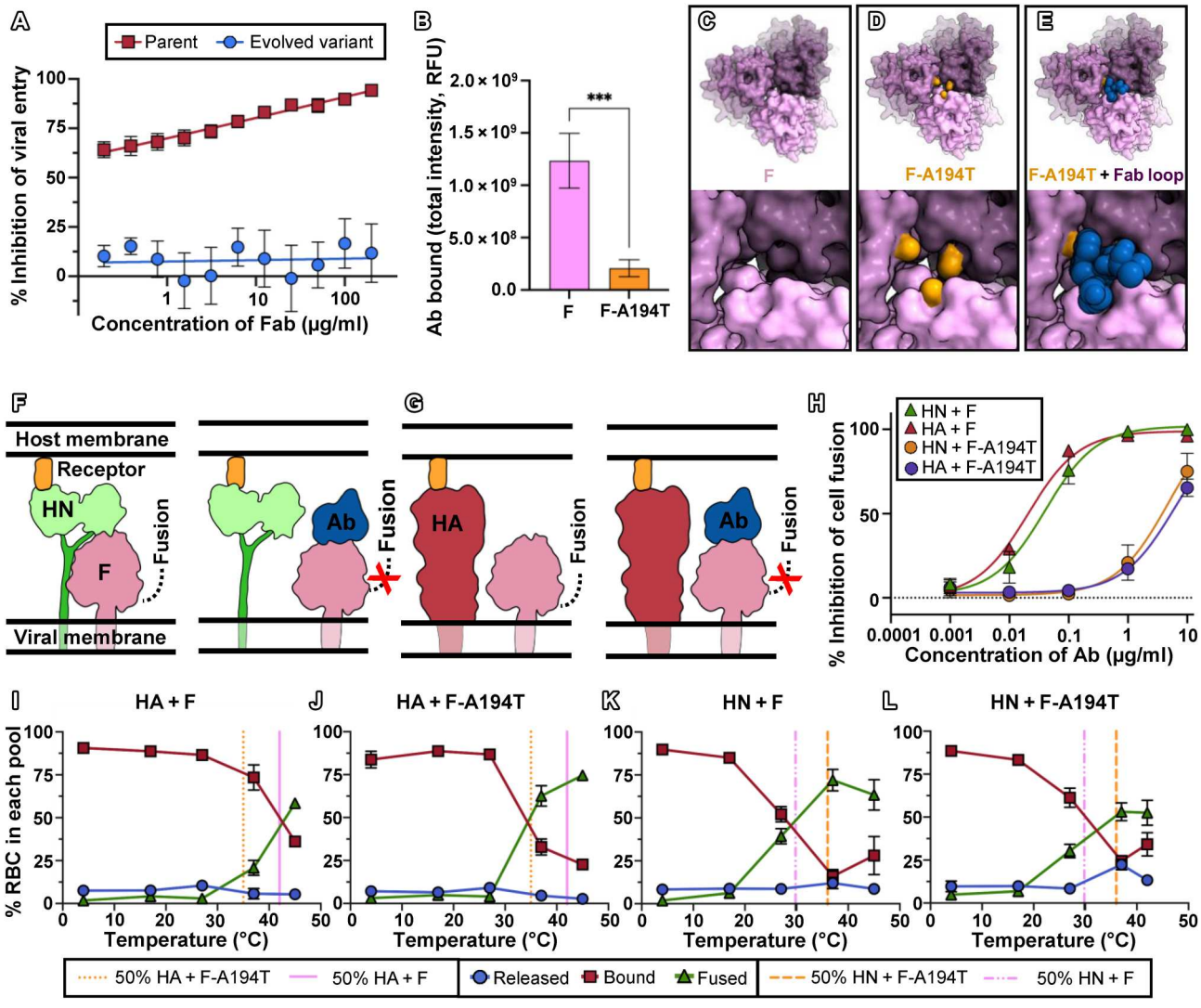

Fig. 5. Alterations at key HN/F interface probed with neutralizing anti-F antibody. (**A**) The virus that arose under selective pressure of PIA174 Fab is resistant to entry inhibition by PIA174 Fab. Inhibition was quantitated by plaque counting normalized to no treatment. (**B**) F-A194T is not recognized by PIA174 Ab on cells expressing F-parental or F-A194T and treated with PIA174 Ab. (**C** to **E**) Top-down view of the soluble cryo-EM prefusion F structure (PDB ID: 6MJZ) for (C) F (pink surface), (D) F with A194T mutation (orange surface), and (E) F-A194T mutation and PIA174 Fab loop (blue spheres). (**F** and **G**) Schematic of glycoprotein combinations used in the next set of experiments: F + HN or F + influenza HA, which tethers via sialic acid receptor engagement but does not complex with, or activate, F, with or without PIA174 Ab. (**H**) Inhibitory activity of PIA174 Ab in cell-cell fusion assay based on α complementation of β-galactosidase (β-Gal) where cell fusion leads to alpha-omega complementation. Receptor-bearing cells coexpressing HN + F (green), HA + F (red), HN + F-A194T (orange), and HA + F-A194T (purple) were treated with PIA174 Ab (*x* axis). *y* axis, % inhibition of fusion by of PIA174 Ab. (**I** and **J**) Activation of F by heat assessed at a range of temperatures without (I) or with (J) F-A194T mutation. Readout for F activation is fusion, binding, or release of red blood cells (RBCs) interacted with the F-expressing cells. (**K** and **L**) Activation of F by HN was assessed at a range of temperatures without (K) or with (L) F-A194T. Data are means ± SE from at least three separate experiments for (A), (B), and (H) to (L).

HPIV3 HN/F complex stably inserted into the viral envelope on the surface of an authentic infectious virion. Here, we examined the state of this complex before receptor engagement, when the prefusion state must be retained intact while the viral envelope is seeking a target cell, provide direct evidence for interaction between the two elements of the fusion complex, and reveal several mechanistic features. We show that HN is present on the viral surface as a dimer, not a tetramer or dimer of dimers, and that the globular heads of each protomer in the HN dimer are rotated with respect to each other, so that one HN head of the dimer is directed downward to contact F, while the other HN head is positioned upward facing above the complex, available to bind to target receptors. We show how HN's downward facing globular domain interacts with the apex of F in a way that suggests a mechanism for stabilizing the prefusion complex.

One of the globular heads of the HN dimer caps the apex of prefusion F and extends a loop downward to interact with a pocket within F. A mutation in this loop (G387S) emerged in patients with persistent HPIV3 infections (*13*), pointing to the biological relevance of this site of HN/F interaction; the HN loop mutation compensated functionally for an HN dimer interface mutation that accelerated viral fusion in this clinical virus. In HPIV3 strains that

emerged during the coronavirus disease 2019 pandemic in South Korea, a loop mutation was identified in HN (*56*), suggesting that properties of the loop may confer some evolutionary advantage. This loop structure, not sequence, is also highly conserved across HN/H/G proteins of paramyxoviruses (Fig. 3, H to J, and fig. S5), implying a general mechanism for maintaining the stability of the prefusion F before receptor engagement (*5*). This remarkable structure suggests the possibility of engineering the F and HN (or G, H for other paramyxoviruses or pneumoviruses) interaction to further stabilize or lock the complex into its prefusion conformation. The resultant stable preactivated fusion complex would likely be an ideal antigen for viral vaccines, because antiviral protection likely requires immunity to this preactivated state of the viral surface glycoprotein (*41*, *57*–*59*).

The HN globular head loop engages a site that overlaps with the epitope of a neutralizing monoclonal antibody that specifically binds the prefusion F, leading to our hypothesis that both the antibody's neutralizing property and HN's stabilizing property derive from interaction at that particular site of F. The finding that the anti–F-neutralizing antibody PIA174 blocks fusion even in the presence of HN suggests that it may displace HN from the F apex (Fig. 5K), as also suggested by the findings that the asymmetric PIA174 Fab antibody fragment inhibited fusion (Fig. 5K), disrupted the HN/F complex (Fig. 4), and maintained stability in the presence of heat (Fig. 4K). The cryo-EM structure of the PIA174/prefusion F complex revealed asymmetric antibody binding to the apex of HPIV3 F at a site known as antigenic site Ø (*10*, *35*). Antibodies that asymmetrically target a similar antigenic site Ø on the fusion proteins of Ebola (GP), respiratory syncytial virus (RSV) (F), HIV-1 (GP120), and human metapneumovirus (HMPV) (F) were found to have higher neutralization potencies compared to symmetrically binding antibodies (*60*–*63*) and were found to stabilize the prefusion state of the fusion proteins (*41*, *57*, *60*, *64*, *65*).

During HPIV3 evolution, under the selective pressure of the anti–F-neutralizing antibody PIA174, two particularly salient mutations emerged—one in F (A194T) at the HN/F loop interface, and the other in HN (H552Q)—that affect the HN/F interaction and the Ab-F interaction. The H552Q mutation in HN affects a residue that we know from previous work to increase receptor avidity, increase HN/F interaction, and increase activation of F (*6*, *11*, *13*, *14*). This mutation, like the A194T mutation in F that allows F to escape Ab recognition and resist activation by HN (Fig. 5, A, B, and H), has also emerged during persistent infection in humans (*13*). The H552Q mutation in HN may have emerged under antibody selection to compensate for the perturbation of HN/F interaction at the F apex by the F A194T mutation, and this idea will be explored. While the escape variant virus bearing the full complement of four escape mutations in HN and F (fig. S8) is fully resistant to neutralization by PIA174 Fab (Fig. 5A), the fusion mediated by F bearing just A194T can be inhibited by the full Ab at high concentrations (Fig. 5H). The difference between Fab and full antibody inhibition, and the contributions of the other three mutations to antibody escape, will be subjects of future study.

The second HN globular head in the dimer points upward so that site I is exposed above the complex and ready to engage a receptor. This binding site is bifunctional and also has a neuraminidase-cleaving or sialidase activity, which is essential for release of progeny virions. The orientation of the HN globular heads that we observe suggests that, in the prereceptor-engaged complex, only one head of the dimer can engage in receptor binding and sialidase activity, while the other is occupied in stabilizing F. While it remains possible that both protomers could bind to receptor moieties, this configuration raises the possibility that upon receptor engagement by one head, the other head is liberated from the F pocket and undergoes a conformational shift.

The structure of the HN/F complex suggests a potential for rotational flexibility between the protomeric heads of HN around the HN dimer interface. Alternate conformations at the HN dimer interface have been observed in crystal structures obtained from soluble forms of HN for NDV (*17*) and PIV5 (*20*). In our viral evolution experiments, mutations at these interface residues are observed during persistent infection in vivo as well as under the selective pressure of growth in culture. These HN dimer interfaces differ from the interface of field strains and may mediate adaptation to different fusion requirements (*6*, *11*–*13*, *36*, *47*). The structural data (Fig. 2) together with this finding of the HN dimer interface hotspot imply a previously unknown step in activation of fusion involving a conformational shift of the HN dimer heads. We hypothesize that the protomer heads rotate upon receptor binding, initiating a signal transferred from one protomer to the other. In support of this notion, the recent cryo-EM structure of the soluble portion of Nipah G suggested a reorientation of domains upon receptor engagement (*66*). Molecular dynamic simulations have shown large rotations between Nipah G protomers after binding to receptor. Our hypothesis is that the axis of rotation between HN heads that we observed (Fig. 2) may serve as a "hinge," permitting rotation of the HN protomer heads with respect to each other and thereby initiating the activation of F after receptor binding, via the F apex site. It is conceivable that receptor engagement provokes this shift of the dimer heads.

The stalk domain of HN is critical for F activation and determines viral specificity (*3*, *27*, *28*), and it is apparent that HN head rotation could induce sliding of the stalk helices with respect to each other. Our results raise the possibility that the specificity of receptor binding protein stalk and fusion protein pairing serves the purpose of providing the proper stalk height to position the receptor binding protein's F-interacting loop at the apex pocket. For paramyxovirus fusion complexes that have been studied, once the receptor binding protein stalk that corresponds to the viral F is provided in a chimeric receptor binding protein, F activation and fusion can be triggered by any one of the viral receptor binding protein globular heads (*4*, *47*, *67*). It seems feasible that the stalk requirement is related to positioning the head interaction correctly. In artificial fusion systems, prefusion F can be induced to activate in the presence of a receptor binding protein that either has no head or has a head positioned high above F (*68*), and fusion can occur. Those findings confirm that if F is stabilized in its prefusion conformation by engineering or by other means, then it can then be artificially activated to fuse by either a stalk or other stimulus [e.g., elevated temperature; (*5*)]. In our viral evolution experiments under the selective pressure of anti–F-neutralizing antibody PIA174 where HN/F interface mutations emerged, a mutation in the HN stalk was also observed; future studies mining these escape variant mutations may shed light on HN stalk–F interaction. The requirements for function of the authentic complex on viral surfaces can now be understood using structure-function correlation in situ of infectious virions.

Several elements of these results reveal shared mechanisms across paramyxoviruses. The structure of the HN loop that interacts

with the apex of F is highly conserved across receptor binding proteins of paramyxoviruses, suggesting a general mechanism for stabilization of the prefusion complex (*5*). We have previously shown that the heads of several paramyxovirus receptor binding proteins can be swapped without affecting the F-activating properties of the receptor binding protein or altering the function of the fusion complex, if the F-complementing stalk is used (*47*, *67*, *69*). For example, Nipah virus F is functional in a complex with a receptor binding protein composed of the Nipah virus G stalk and an NDV HN head (*4*, *67*), measles virus F is functional in a complex with a receptor binding protein composed of the measles H stalk and an HPIV3 HN head (*69*, *70*), and HPIV3 F can complex with and mediate fusion when paired with an HPIV3 HN stalk and NDV HN globular head (*47*), indicating that a shared mechanism operates across multiple paramyxovirus receptor binding protein heads. Despite the complete lack of sequence homology between these viral receptor binding proteins, the interaction between the downward loop on the head of HN and the apex of F is a highly conserved structure (Fig. 3, H to J, and fig. S5). The use of cryo-ET to obtain subnanometer resolution of the HN/F complex of HPIV3 on the virus′ surface, the first such in situ structure of an asymmetric viral fusion complex, reveals prefusion HN/F interactions that have key implications for the mechanism of fusion. The HN/F loop-pocket interface identified here could offer a new broad paramyxovirus antiviral target site.

MATERIALS AND METHODS

Virus growth and purification

Recombinant viruses were generated by reverse genetics as previously described using an HPIV3 CI-1-EGFP (enhanced green fluorescent protein) background and a recombinant, clinically isolated (CI-1) HPIV3 virus sequence containing an EGFP cassette between genes P and M. Resulting viruses were propagated using the human airway epithelial (HAE) EpiAirway AIR-100 system (MatTek Corporation) and harvested in 1× phosphate-buffered saline (PBS) with magnesium and calcium (MatTek Corporation). HAE supernatant fluid was subsequently collected and clarified by low-speed centrifugation (1800 relative centrifugal force for 10 min at 4°C). Viruses were titered by limiting dilution infection of Vero cells [the American Type Culture Collection (ATCC)], and infected cells were quantified using an IN Cell Analyzer 2000. All recombinant viruses were sequenced using metagenomic next-generation sequencing (mNGS) as previously described (*71*) before experimental use.

Chemicals and antibodies

Zanamivir (Acme Bioscience) was dissolved in Opti-MEM at a concentration of 50 mM and stored at −80°C. Monoclonal anti-HPIV3 HN antibodies were custom elicited in rats (Aldevron) using eGFP-HN complementary DNA, diluted in Dulbecco′s PBS (DPBS) to 100 μg/ml, and kept at 4°C. PIA174 antibody fragment (Fab) and full antibody (Ab) were purchased from Creative Biolabs. PA3/F4 was purified by Rockland Immunochemicals Inc. and was originally generated as described in (*46*).

Cryo-ET preparation HN and F complex

Lacey carbon gold grids, containing a continuous layer of thin carbon (Ted Pella), were plasma cleaned with Fischione M1070 NanoClean on 70% power for 20 s with a 25% oxygen and 75% argon gas mixture. Eight-microliter drops, containing the anti-HPIV3 HN antibody (100 μg/ml), were incubated on the grids for 10 min, and then, the grids were washed with DPBS to remove unabsorbed antibodies. Next, grids were blotted and placed face down in the HAE supernatant fluid, containing in a six-well plate. Plates were incubated for 30 min at 4°C with rocking. For the prefusion F Fab bound to prefusion F subtomogram averaging experiments, grids were subjected to another 30-min incubation at 4°C with rocking in the presence of a PIA174 Fab (10 μg/ml; Creative Biolabs) concentration. After incubation in the supernatant fluid, the grids were washed in cold DPBS 15 times. Grids were then washed in a DPBS solution containing 5-nm gold nanoparticles (Sigma-Aldrich) added at a 10% concentration of the final solution. Grids were then plunge frozen in liquid ethane, using a Vitrobot (Mark IV; Thermo Fisher Scientific Co.). For negative controls, we applied an antibody specific for measles H to the grids and did not observe viral particles on these grids.

Cryo-ET collection for subtomogram averaging

Vitrified grids were imaged using a Titan Halo 300-kV transmission electron microscope (Thermo Fisher Scientific Co.) and equipped with a Gatan K3 direct detector and no energy filter. Images were captured at a magnification of ×18,000, giving a pixel size of 1.72 Å at the specimen level. Images were acquired with SerialEM software (*72*) with a 3.5- to 5.0-μm defocus and a bidirectional tilt series of 3° steps starting from −9° to 51° and then −12° to −51°. Each tilt had a dose of 3.4 $e^{-}/Å^2$, resulting in a total dose of ~100 $e^{-}/Å^2$ for the tilt series.

Cryo-ET image processing

All micrograph movies were aligned using WarpEM (*38*). Tilt series were aligned with Etomo (*73*), and then, the aligned parameters were used to reconstruct the contrast transfer function (CTF)-corrected tomograms in WarpEM. Eleven tomograms for the HN/F complex and six tomograms for the prefusion F antibody bound to F were selected for subtomogram averaging.

Cryo-ET image processing for the HN/F complex

The subtomogram averaging process was performed using the Dynamo software package (*74*). Subvolumes of the viral particle surfaces (440) $Å^3$ were extracted from 2× binned tomograms. The first round of reference free alignment was followed by centering and recropping to (316) $Å^3$ on a density corresponding to an HN and F complex. A second round of six iterations with a 360° azimuth range on these centered particles was performed with an initial reference of an HN (PDB ID: 4MZA) and F (PDB ID: 6MJZ) model prefiltered to 30 Å and a cylindrical mask including the membrane. Iterations in rounds 2 to 5 had an initial reference that was low-pass–filtered to 30 Å and came from the previous rounds average. Subvolumes in rounds 3 to 5 (18 iterations) were aligned with decreasing of the azimuth range from 120° to 15° in the presence of cylindrical mask, encompassing only the HN and F density. Overlapping particles with less than 60 Å of separation were removed in the fifth round, and particles with the highest cross correlation were selected for reextraction of subtomograms binned 1× using Warp with a box size of (184) $Å^3$. Subvolumes were then subjected to two more rounds of refinement with azimuth range of 15° and 5° steps with a tight mask surrounding HN and F and generated with

the mask creation tool in Relion (*75*). Subvolumes were subjected to one round of focused refinement with either an HN- or F-focused mask generated in Relion (*75*), resulting in a calculated resolution of 10.2 Å at 0.143-Å cutoff value. Resolution for the resulting maps was estimated by FSC with a 0.143-Å cutoff value using three-dimensional FSC (3DFSC) (*76*). Resolutions were estimated to be 8.5 Å for HN and 9.3 Å for F, and these subtomogram averages were combined for the final map using Chimera (*77*). For the HN overview subtomogram averaging, subvolumes of the viral particle surfaces (550) $Å^3$ were extracted using the final HN/F complex coordinates from 2× binned tomograms. A round of 12 iterations with a 45° azimuth range on these centered particles was performed with an initial reference that was low-pass–filtered to 30 Å and came from the previous rounds average. Subvolumes were aligned with in the presence of cylindrical mask, encompassing only the HN canopy density. These subvolumes were then subjected to classification using the Dynamo software package through principal components analysis.

Cryo-ET image processing for the prefusion F Fab bound to F

The subtomogram averaging process was performed using the Dynamo software package (*74*). Subvolumes of the viral particle surfaces (330) $Å^3$ were extracted from 2× binned tomograms. The first round of reference free alignment was followed by a second round of centering all particles to a 30-Å low-pass F (PDB ID: 6MJZ) complex with a resolution limit of 30 Å imposed in each iteration. A cylindrical mask including the membrane was imposed along with a 360° azimuth range. Subvolume alignment in rounds 3 to 5 was implemented with successive decrease of the azimuth range from 120° to 15° in the presence of cylindrical mask, encompassing the prefusion F bound to Fab fragment. Overlapping particles with less than 60 Å of separation were removed in the fifth round, and particles with the highest cross correlation were selected. Subvolumes were then subjected to two more rounds of refinement with azimuth range of 15° and 5° steps with a tight mask surrounding HN and F generated with the mask creation tool in Relion (*75*). The final volume obtained had a resolution of 16.51 Å for the complex at the 0.143-Å cutoff value.

Model fitting and image analysis

All cryo-EM movie images were visualized using ImageJ, IMOD (*78*), ChimeraX (*79*), and Chimera (*77*). FSCs performed by 3DFSC (*76*), Mtriage (*80*), and ResMap (*81*) were used to validate the final resolution. The number of particles included in the analysis and the strategy used are summarized in fig. S2. Model fitting and model-to-map cross-correlation fit was performed in Chimera (*77*) and ChimeraX (*79*) using the protomers from the crystal structure of HN (PDB ID: 4MZA) and cryo-EM structure of F solved with prefusion F Fab antibody fragment (PDB ID: 6MJZ). The axis of rotations for both NDV (PDB IDs: 1E8V and 1E8U) and HPIV3 (PDB ID: 4MZA; cryo-ET model) were calculated and visualized in PyMOL (Schrödinger LLC). Buried surface area in HN dimer interface was calculated in Chimera.

AlphaFold2 model fitting and image analysis

Using ColabFold, a straightforward input complex prediction software for AlphaFold2 (https://colab.research.google.com/github/sokrypton/ColabFold/blob/main/AlphaFold2.ipynb) (*39*, *40*), the full-length HN sequence was input as a dimer with an output of five structural model PDBs. These PDBs were visualized in ChimeraX (*79*). For the stalk region of F, ColabFold was used, and the top scoring trimer was merged with the soluble prefusion F structure using Chimera (*77*).

Statistics

Statistical analysis was performed where appropriate using GraphPad Prism 9 and two-way analysis of variance (ANOVA). Results are means ± SEM unless otherwise stated. *P* values less than 0.05 were considered statistically significant.

Glycoprotein cross-linking

Monolayers of human embryonic kidney (HEK) 293T cells transiently expressing HPIV3 F and either HPIV3 HN or empty vector were treated with 2 mM zanamivir in complete medium to prevent cell-cell fusion during overnight incubation at 37°C. After 16 hours, cells were brought to 4°C, incubated for 30 min, with or without DTSSP 1 mM, and then treated with varying concentrations (10, 5, 1, 0.2, 0.04, 0.008, and 0.0016 μg/ml) of PIA174 prefusion F Fab that had been labeled with a Biotium Mix-n-Stain cyanine-based fluorescent (CF) dye antibody labeling kit. After incubation with labeled PIA174 prefusion F Fab for 1 hour on ice, cells were washed, fixed with 4% paraformaldehyde (PFA), treated with DAPI (4′,6-diamidino-2-phenylindole; 1 μg/ml), and imaged on an IN Cell Analyzer 2000 fluorescein isothiocyanate channel. Analysis was performed on a CellProfiler by quantifying the number of green cells divided by the number of DAPI-positive cells. All results were normalized to the value of F alone at the highest concentration.

F stability assay

To detect the prefusion conformation of F, monolayers of 293T cells transiently expressing HPIV3 F in a 96-well plate were equilibrated at 4°C for 15 min and then subjected to 55°C for 5, 15, 30, or 60 min in the absence or presence of PIA174 F Fab (1 μg/ml). For cells not treated with PIA174, the Fab was added after cells were placed on ice. For staining, anti-human H+L (0.5 μg/ml) conjugated with DyLight 594 (Abcam) and DAPI (1 μg/ml; Fisher Scientific Co.) was added. After imaging on Cytation 5 (BioTek), percent positive cells were calculated by automated counting of Fab-positive cells/DAPI-positive cells. Percent positive (prefusion F) was normalized to the value of F alone incubated with Fab at 4°C. To detect the postfusion conformation of F, monolayers of 293T cells transiently expressing HPIV3 F protein in a 96-well plate were equilibrated at 4°C and then subjected to 55°C for 30 min in the absence or presence of prefusion PIA174 F antibody (1 μg/ml). Postfusion F was detected with anti-postfusion F antibody [8.5 μg/ml; PA3/F4 (*46*); purified by Rockland Immunochemicals Inc.] followed by anti-mouse immunoglobulin G (2 μg/ml) conjugated with Alexa Fluor Plus 488 (Invitrogen) mixed with DAPI (1 μg/ml; Fisher Scientific Co.). Fluorescence intensity was determined by imaging on Cytation 5 (BioTek). Total GFP fluorescence intensity was normalized to the value of the no treatment group incubated at 55°C for 30 min.

Viral evolution experiments

Vero cells (ATCC) in a 96-well plate were infected with 200 plaque-forming units (PFUs) per well of HPIV3 expressing mCherry [modified from (*82*), a gift from U. Buchholz and P. Collins, National

Institute of Allergy and Infectious Diseases] in Opti-MEM (Gibco, 31985070) supplemented with 1% penicillin-streptomycin. After 2 hours, the infection medium was replaced with decreasing concentrations of PIA174 antibody (10 μg/ml; 1:2 dilutions down to 0.04 μg/ml). Because significant viral spread was observed in all wells after 2 days, this virus was passaged onto new cells with four times higher concentration of antibody (40 μg/ml; 1:2 dilutions to 0.16 μg/ml). Infection was monitored, and antibody was replaced every 2 days. Virus was collected and frozen at −80°C on days 1, 3, 4, 6, and 7 after infection. After day 7, putative escape mutants (observed exponential growth in wells at the highest concentration of antibody) were propagated in Vero cells in the presence of selective concentration of antibody (4 μg/ml) in a T-25 flask. These viruses, and control viruses that were passaged alongside mutant viruses without antibody, were sequenced.

Sequencing library analysis

Shotgun RNA sequencing metagenomic reads (*71*) were adapter- and Q20 quality–trimmed using Trimmomatic v0.39 (*83*). Variants for all samples were called using the reference-based options in LAVA (https://github.com/greninger-lab/lava). Briefly, shotgun RNA sequencing reads for the viral genome from the virus that escaped during the viral evolution experiment were aligned to the reference sequence for the HPIV3 expressing mCherry (GenBank accession no. OP821798) using bwa-mem v0.7.17-r1188 (https://arxiv.org/abs/1303.3997), and variant allele frequencies were extracted using bcftools v1.9 (*84*) and annotated via VarScan v2.3 (*85*). Sequencing reads are available in NCBI BioProject PRJNA901026.

Plaque reduction assay

Vero cells (ATCC) in a 96-well plate were infected with 500 PFUs per well of parental or escape variant virus in the presence of a range of concentrations of PIA174 Fab (200 μg/ml; 1:2 dilution to ~0.2 μg/ml) and incubated for 2 hours at 37°C. Then, the antibody was removed, and the cells overlaid with 0.5% carboxymethyl cellulose. After 18 hours, cells were imaged on a Cytation 5 imager, and fluorescently labeled cells were counted. Inhibition of entry was quantified by comparing the number of infected cells at different concentrations of antibody to the number of infected cells in the absence of antibody for each virus.

Antibody binding

HEK-293T cells were transiently transfected with HPIV3 F or HPIV3 F bearing A194T and incubated for 18 hours at 37°C. The cells were then washed, treated with PIA174 antibody (1 μg/ml) for 1 hour at 4°C, washed again, treated with secondary anti-human conjugated with DyLight 594 (0.5 μg/ml) for 30 min at 4°C, fixed with 4% PFA, and treated with DAPI (2 μg/ml). Cells were then imaged on a Cytation 5 imager, and the total intensity per well was measured.

β-Gal complementation-based fusion assay to assess antibody inhibition

We previously adapted a fusion assay based on α complementation of β-galactosidase (β-Gal) (*11*). In this assay, receptor-bearing cells expressing the omega peptide of β-Gal are mixed with cells coexpressing envelope glycoproteins and the α peptide of β-Gal, and cell fusion leads to complementation. Fusion is stopped by lysing the cells. Substrate was added (Galacton-Star substrate; Applied Biosystems, T1012), and luminescence was read after 1 hour at 500 ms on a Tecan M1000 Pro. Percent inhibition was quantified by comparing relative luminescence units (RLUs) at different concentrations of antibody to RLUs in the absence of antibody 100 × [1 − (luminescence at *X* background)/(luminescence in the absence of inhibitor − background)].

Measurement of F-activation and fusion between RBCs and envelope glycoprotein-expressing cells

Monolayers of 293T cells transiently expressing viral glycoproteins (treated overnight with 25 mU per well neuraminidase) were washed and incubated with 1% RBC suspensions (pH 7.5) for 30 min at 4°C. After the samples were rinsed to remove unbound RBCs, they were placed at 37°C for the indicated time with or without 2 mM zanamivir (pH 8.0). The plates were then rocked, and the liquid phase was collected in V-bottom tubes for measurement of released RBCs. The cells were then incubated at 4°C with 200 μl of RBC lysis solution (ammonium-chloride-potassium lysis buffer; Thermo Fisher Scientific, A1049201), where the lysis of unfused RBCs removes RBCs that have not fused with cells coexpressing envelope glycoproteins. The liquid phase was collected in V-bottom 96-well plates for measurement of bound RBCs. The cells were then lysed in 200 μl of dodecyl maltoside HEPES (DH) buffer [5 mM Hepes, 10 mM NaCl, and dodecyl maltoside (0.5 mg/ml)] 1:10 in PBS and transferred to flat-bottom 96-well plates for quantification of fused RBCs. The amount of RBCs in each of the above three compartments was determined by measuring the absorption at 405 nm.

Supplementary Materials

This PDF file includes:
Figs. S1 to S8
Legends for movies S1 to S4

Other Supplementary Material for this manuscript includes the following:
Movies S1 to S4

View/request a protocol for this paper from *Bio-protocol*.

REFERENCES AND NOTES

1. T. C. Marcink, M. Porotto, A. Moscona, Parainfluenza virus entry at the onset of infection. *Adv. Virus Res.* **111**, 1–29 (2021).
2. A. Moscona, R. W. Peluso, Fusion properties of cells persistently infected with human parainfluenza virus type 3: Participation of hemagglutinin-neuraminidase in membrane fusion. *J. Virol.* **65**, 2773–2777 (1991).
3. M. Porotto, M. Murrell, O. Greengard, A. Moscona, Triggering of human parainfluenza virus 3 fusion protein (F) by the hemagglutinin-neuraminidase (HN) protein: An HN mutation diminishes the rate of F activation and fusion. *J. Virol.* **77**, 3647–3654 (2003).
4. M. Porotto, I. DeVito, S. G. Palmer, E. M. Jurgens, J. L. Yee, C. C. Yokoyama, A. Pessi, A. Moscona, Spring-loaded model revisited: Paramyxovirus fusion requires engagement of a receptor binding protein beyond initial triggering of the fusion protein. *J. Virol.* **85**, 12867–12880 (2011).
5. M. Porotto, Z. W. Salah, L. Gui, I. DeVito, E. M. Jurgens, H. Lu, C. C. Yokoyama, L. M. Palermo, K. K. Lee, A. Moscona, Regulation of paramyxovirus fusion activation: The hemagglutinin-neuraminidase protein stabilizes the fusion protein in a pretriggered state. *J. Virol.* **86**, 12838–12848 (2012).
6. R. Xu, S. G. Palmer, M. Porotto, L. M. Palermo, S. Niewiesk, I. A. Wilson, A. Moscona, Interaction between the hemagglutinin-neuraminidase and fusion glycoproteins of human parainfluenza virus type III regulates viral growth *in vivo*. *MBio* **4**, e00803–e00813 (2013).

7. T. C. Marcink, T. Wang, A. des Georges, M. Porotto, A. Moscona, Human parainfluenza virus fusion complex glycoproteins imaged in action on authentic viral surfaces. *PLOS Pathog.* **16**, e1008883 (2020).
8. A. Chang, R. E. Dutch, Paramyxovirus fusion and entry: Multiple paths to a common end. *Viruses* **4**, 613–636 (2012).
9. A. Scheid, P. Choppin, Identification of biological activities of paramyxovirus glycoproteins. Activation of cell fusion, hemolysis, and infectivity by proteolytic cleavage of an inactive precursor protein of Sendai virus. *Virology* **57**, 475–490 (1974).
10. G. B. E. Stewart-Jones, G.-Y. Chuang, K. Xu, T. Zhou, P. Acharya, Y. Tsybovsky, L. Ou, B. Zhang, B. Fernandez-Rodriguez, V. Gilardi, C. Silacci-Fregni, M. Beltramello, U. Baxa, A. Druz, W. P. Kong, P. V. Thomas, Y. Yang, K. E. Foulds, J.-P. Todd, H. Wei, A. M. Salazar, D. G. Scorpio, B. Carragher, C. S. Potter, D. Corti, J. R. Mascola, A. Lanzavecchia, P. D. Kwong, Structure-based design of a quadrivalent fusion glycoprotein vaccine for human parainfluenza virus types 1–4. *Proc. Natl. Acad. Sci. U.S.A.* **115**, 12265–12270 (2018).
11. M. Porotto, M. Fornabaio, G. E. Kellogg, A. Moscona, A second receptor binding site on human parainfluenza virus type 3 hemagglutinin-neuraminidase contributes to activation of the fusion mechanism. *J. Virol.* **81**, 3216–3228 (2007).
12. S. Iketani, R. C. Shean, M. Ferren, N. Makhsous, D. B. Aquino, A. des Georges, B. Rima, C. Mathieu, M. Porotto, A. Moscona, A. L. Greninger, Viral entry properties required for fitness in humans are lost through rapid genomic change during viral isolation. *MBio* **9**, e00898–e00818 (2018).
13. A. L. Greninger, K. Rybkina, M. J. Lin, J. Drew-Bear, T. C. Marcink, R. C. Shean, N. Makhsous, M. Boeckh, O. Harder, F. Bovier, S. R. Burstein, S. Niewiesk, B. K. Rima, M. Porotto, A. Moscona, Human parainfluenza virus evolution during lung infection of immunocompromised individuals promotes viral persistence. *J. Clin. Invest.* **131**, e150506 (2021).
14. M. Porotto, S. G. Palmer, L. M. Palermo, A. Moscona, Mechanism of fusion triggering by human parainfluenza virus type III: Communication between viral glycoproteins during entry. *J. Biol. Chem.* **287**, 778–793 (2012).
15. N. Ader-Ebert, M. Khosravi, M. Herren, M. Avila, L. Alves, F. Bringolf, C. Örvell, J. P. Langedijk, A. Zurbriggen, R. K. Plemper, P. Plattet, Sequential conformational changes in the morbillivirus attachment protein initiate the membrane fusion process. *PLOS Pathog.* **11**, e1004880 (2015).
16. P. Plattet, R. K. Plemper, Envelope protein dynamics in paramyxovirus entry. *MBio* **4**, e00413 (2013).
17. S. Crennell, T. Takimoto, A. Portner, G. Taylor, Crystal structure of the multifunctional paramyxovirus hemagglutinin-neuraminidase. *Nat. Struct. Biol.* **7**, 1068–1074 (2000).
18. K. A. Baker, R. E. Dutch, R. A. Lamb, T. S. Jardetzky, Structural basis for paramyxovirus-mediated membrane fusion. *Mol. Cell* **3**, 309–319 (1999).
19. M. C. Lawrence, N. A. Borg, V. A. Streltsov, P. A. Pilling, V. C. Epa, J. N. Varghese, J. L. Mc Kimm-Breschkin, P. M. Colman, Structure of the Haemagglutinin-neuraminidase from human parainfluenza virus type III. *J. Mol. Biol.* **335**, 1343–1357 (2004).
20. S. Bose, T. S. Jardetzky, R. A. Lamba, Timing is everything: Fine-tuned molecular machines orchestrate paramyxovirus entry. *Virology* **479**, 518–531 (2015).
21. Z. Ke, J. D. Strauss, C. M. Hampton, M. A. Brindley, R. S. Dillard, F. Leon, K. M. Lamb, R. K. Plemper, E. R. Wright, Promotion of virus assembly and organization by the measles virus matrix protein. *Nat. Commun.* **9**, 1736 (2018).
22. L. Liljeroos, M. A. Krzyzaniak, A. Helenius, S. J. Butcher, Architecture of respiratory syncytial virus revealed by electron cryotomography. *Proc. Natl. Acad. Sci. U.S.A.* **110**, 11133–11138 (2013).
23. C. C. Stobart, C. A. Rostad, Z. Ke, R. S. Dillard, C. M. Hampton, J. D. Strauss, H. Yi, A. L. Hotard, J. Meng, R. J. Pickles, K. Sakamoto, S. Lee, M. G. Currier, S. M. Moin, B. S. Graham, M. S. Boukhvalova, B. E. Gilbert, J. C. G. Blanco, P. A. Piedra, E. R. Wright, M. L. Moore, A live RSV vaccine with engineered thermostability is immunogenic in cotton rats despite high attenuation. *Nat. Commun.* **7**, 13916 (2016).
24. Y. H. Kim, J. E. Donald, G. Grigoryan, G. P. Leser, A. Y. Fadeev, R. A. Lamb, W. F. DeGrado, Capture and imaging of a prehairpin fusion intermediate of the paramyxovirus PIV5. *Proc. Natl. Acad. Sci. U.S.A.* **108**, 20992–20997 (2011).
25. S. Bose, B. D. Welch, C. A. Kors, P. Yuan, T. S. Jardetzky, R. A. Lamb, Structure and mutagenesis of the parainfluenza virus 5 hemagglutinin-neuraminidase stalk domain reveals a four-helix bundle and the role of the stalk in fusion promotion. *J. Virol.* **85**, 12855–12866 (2011).
26. M. Porotto, M. Murrell, O. Greengard, L. Doctor, A. Moscona, Influence of the human parainfluenza virus 3 attachment protein's neuraminidase activity on its capacity to activate the fusion protein. *J. Virol.* **79**, 2383–2392 (2005).
27. R. Deng, Z. Wang, A. M. Mirza, R. M. Iorio, Localization of a domain on the paramyxovirus attachment protein required for the promotion of cellular fusion by its homologous fusion protein spike. *Virology* **209**, 457–469 (1995).
28. K. Tanabayashi, R. W. Compans, Functional interaction of paramyxovirus glycoproteins: Identification of a domain in Sendai virus HN which promotes cell fusion. *J. Virol.* **70**, 6112–6118 (1996).
29. V. Zaitsevet, M. von Itzstein, D. Groves, M. Kiefel, T. Takimoto, A. Portner, G. Taylor, Second sialic acid binding site in newcastle disease virus hemagglutinin-neuraminidase: Implications for fusion. *J. Virol.* **78**, 3733–3741 (2004).
30. H.-S. Yin, X. Wen, R. G. Paterson, R. A. Lamb, T. S. Jardetzky, Structure of the parainfluenza virus 5 F protein in its metastable, prefusion conformation. *Nature* **439**, 38–44 (2006).
31. D. Wrapp, N. Wang, K. S. Corbett, J. A. Goldsmith, C.-L. Hsieh, O. Abiona, B. S. Graham, J. S. McLellan, Cryo-EM structure of the 2019-nCoV spike in the prefusion conformation. *Science* **367**, 1260–1263 (2020).
32. J. E. Lee, M. L. Fusco, A. J. Hessell, W. B. Oswald, D. R. Burton, E. O. Saphire, Structure of the Ebola virus glycoprotein bound to an antibody from a human survivor. *Nature* **454**, 177–182 (2008).
33. D. J. Benton, S. J. Gamblin, P. B. Rosenthal, J. J. Skehel, Structural transitions in influenza haemagglutinin at membrane fusion pH. *Nature* **583**, 150–153 (2020).
34. J. H. Lee, G. Ozorowski, A. B. Ward, Cryo-EM structure of a native, fully glycosylated, cleaved HIV-1 envelope trimer. *Science* **351**, 1043–1048 (2016).
35. J. Boonyaratanakornkit, S. Singh, C. Weidle, J. Rodarte, R. Bakthavatsalam, J. Perkins, G. B. E. Stewart-Jones, P. D. Kwong, A. T. McGuire, M. Pancera, J. J. Taylor, Protective antibodies against human parainfluenza virus type 3 infection. *MAbs* **13**, 1912884 (2021).
36. S. G. Palmer, M. Porotto, L. M. Palermo, L. F. Cunha, O. Greengard, A. Moscona, Adaptation of human parainfluenza virus to airway epithelium reveals fusion properties required for growth in host tissue. *mBio* **3**, e00137–e00112 (2012).
37. S. G. Palmer, I. DeVito, S. G. Jenkins, S. Niewiesk, M. Porotto, A. Moscona, Circulating clinical strains of human parainfluenza virus reveal viral entry requirements for in vivo infection. *J. Virol.* **88**, 13495–13502 (2014).
38. D. Tegunov, L. Xue, C. Dienemann, P. Cramer, J. Mahamid, Multi-particle cryo-EM refinement with M visualizes ribosome-antibiotic complex at 3.5 Å in cells. *Nat. Methods* **18**, 186–193 (2021).
39. M. Varadi, S. Anyango, M. Deshpande, S. Nair, C. Natassia, G. Yordanova, D. Yuan, O. Stroe, G. Wood, A. Laydon, A. Žídek, T. Green, K. Tunyasuvunakool, S. Petersen, J. Jumper, E. Clancy, R. Green, A. Vora, M. Lutfi, M. Figurnov, A. Cowie, N. Hobbs, P. Kohli, G. Kleywegt, E. Birney, D. Hassabis, S. Velankar, AlphaFold protein structure database: Massively expanding the structural coverage of protein-sequence space with high-accuracy models. *Nucleic Acids Res.* **50**, D439–D444 (2022).
40. J. Jumper, R. Evans, A. Pritzel, T. Green, M. Figurnov, O. Ronneberger, K. Tunyasuvunakool, R. Bates, A. Žídek, A. Potapenko, A. Bridgland, C. Meyer, S. A. A. Kohl, A. J. Ballard, A. Cowie, B. Romera-Paredes, S. Nikolov, R. Jain, J. Adler, T. Back, S. Petersen, D. Reiman, E. Clancy, M. Zielinski, M. Steinegger, M. Pacholska, T. Berghammer, S. Bodenstein, D. Silver, O. Vinyals, A. W. Senior, K. Kavukcuoglu, P. Kohli, D. Hassabis, Highly accurate protein structure prediction with AlphaFold. *Nature* **596**, 583–589 (2021).
41. M. B. Battles, V. Más, E. Olmedillas, O. Cano, M. Vázquez, L. Rodríguez, J. A. Melero, J. S. McLellan, Structure and immunogenicity of pre-fusion-stabilized human metapneumovirus F glycoprotein. *Nat. Commun.* **8**, 1528 (2017).
42. T. Hashiguchi, Y. Fukuda, R. Matsuoka, D. Kuroda, M. Kubota, Y. Shirogane, S. Watanabe, K. Tsumoto, D. Kohda, R. K. Plemper, Y. Yanagi, Structures of the prefusion form of measles virus fusion protein in complex with inhibitors. *Proc. Natl. Acad. Sci. U.S.A.* **115**, 2496–2501 (2018).
43. I. Rossey, M. S. A. Gilman, S. C. Kabeche, K. Sedeyn, D. Wrapp, M. Kanekiyo, M. Chen, V. Mas, J. Spitaels, J. A. Melero, B. S. Graham, B. Schepens, J. S. McLellan, X. Saelens, Potent single-domain antibodies that arrest respiratory syncytial virus fusion protein in its prefusion state. *Nat. Commun.* **8**, 14158 (2017).
44. N. Duro, S. Varma, Role of structural fluctuations in allosteric stimulation of paramyxovirus hemagglutinin-neuraminidase. *Structure* **27**, 1601–1611.e2 (2019).
45. L. Dirr, I. M. El-Deeb, L. M. G. Chavas, P. Guillon, M. von Itzstein, The impact of the butterfly effect on human parainfluenza virus haemagglutinin-neuraminidase inhibitor design. *Sci. Rep.* **7**, 4507 (2017).
46. S. F. Bottom-Tanzer, K. Rybkina, J. N. Bell, C. A. Alabi, C. Mathieu, M. Lu, S. Biswas, M. Vasquez, M. Porotto, J. A. Melero, V. Más, A. Moscona, Inhibiting human parainfluenza virus infection by preactivating the cell entry mechanism. *MBio* **10**, e02900–e02918 (2019).
47. M. Porotto, Z. Salah, I. DeVito, A. Talekar, S. G. Palmer, R. Xu, I. A. Wilson, A. Moscona, The second receptor binding site of the globular head of the Newcastle disease virus hemagglutinin-neuraminidase activates the stalk of multiple paramyxovirus receptor binding proteins to trigger fusion. *J. Virol.* **86**, 5730–5741 (2012).
48. M. Porotto, M. Fornabaio, O. Greengard, M. T. Murrell, G. E. Kellogg, A. Moscona, Paramyxovirus receptor-binding molecules: Engagement of one site on the hemagglutinin-

neuraminidase protein modulates activity at the second site. *J. Virol.* **80**, 1204–1213 (2006).
49. S. A. Connolly, G. P. Leser, T. S. Jardetzky, R. A. Lamb, Bimolecular complementation of paramyxovirus fusion and hemagglutinin-neuraminidase proteins enhances fusion: Implications for the mechanism of fusion triggering. *J. Virol.* **83**, 10857–10868 (2009).
50. C. K. Navaratnarajah, N. Oezguen, L. Rupp, L. Kay, V. H. J. Leonard, W. Braun, R. Cattaneo, The heads of the measles virus attachment protein move to transmit the fusion-triggering signal. *Nat. Struct. Mol. Biol.* **18**, 128–134 (2011).
51. Z. Li, W. Li, M. Lu, J. Bess Jr., C. W. Chao, J. Gorman, D. S. Terry, B. Zhang, T. Zhou, S. C. Blanchard, P. D. Kwong, J. D. Lifson, W. Mothes, J. Liu, Subnanometer structures of HIV-1 envelope trimers on aldrithiol-2-inactivated virus particles. *Nat. Struct. Mol. Biol.* **27**, 726–734 (2020).
52. V. Mangala Prasad, P. Leaman, K. N. Lovendahl, J. T. Croft, M. A. Benhaim, E. A. Hodge, M. B. Zwick, K. K. Lee, Cryo-ET of Env on intact HIV virions reveals structural variation and positioning on the Gag lattice. *Cell* **185**, 641–53.e17 (2022).
53. H. Yao, Y. Song, Y. Chen, N. Wu, J. Xu, C. Sun, J. Zhang, T. Weng, Z. Zhang, Z. Wu, L. Cheng, D. Shi, X. Lu, J. Lei, M. Crispin, Y. Shi, L. Li, S. Li, Molecular architecture of the SARS-CoV-2 virus. *Cell* **183**, 730–738.e13 (2020).
54. Z. Ke, J. Oton, K. Qu, M. Cortese, V. Zila, L. McKeane, T. Nakane, J. Zivanov, C. J. Neufeldt, B. Cerikan, J. M. Lu, J. Peukes, X. Xiong, H.-G. Kräusslich, S. H. W. Scheres, R. Bartenschlager, J. A. G. Briggs, Structures and distributions of SARS-CoV-2 spike proteins on intact virions. *Nature* **588**, 498–502 (2020).
55. B. Turoňová, M. Sikora, C. Schürmann, W. J. H. Hagen, S. Welsch, F. E. C. Blanc, S. von Bülow, M. Gecht, K. Bagola, C. Hörner, G. van Zandbergen, J. Landry, N. T. D. de Azevedo, S. Mosalaganti, A. Schwarz, R. Covino, M. D. Mühlebach, G. Hummer, J. K. Locker, M. Beck, In situ structural analysis of SARS-CoV-2 spike reveals flexibility mediated by three hinges. *Science* **370**, 203–208 (2020).
56. H. N. Kim, S.-Y. Yoon, C. S. Lim, C. K. Lee, J. Yoon, Phylogenetic analysis of human parainfluenza type 3 virus strains responsible for the outbreak during the COVID-19 pandemic in Seoul, South Korea. *J. Clin. Virol.* **153**, 105213 (2022).
57. J. O. Ngwuta et al., Prefusion F–specific antibodies determine the magnitude of RSV neutralizing activity in human sera. *Sci. Transl. Med.* **7**, 309ra162 (2015).
58. J. S. McLellan, M. Chen, M. G. Joyce, M. Sastry, G. B. E. Stewart-Jones, Y. Yang, B. Zhang, L. Chen, S. Srivatsan, A. Zheng, T. Zhou, K. W. Graepel, A. Kumar, S. Moin, J. C. Boyington, G.-Y. Chuang, C. Soto, U. Baxa, A. Q. Bakker, H. Spits, T. Beaumont, Z. Zheng, N. Xia, S.-Y. Ko, J.-P. Todd, S. Rao, B. S. Graham, P. D. Kwong, Structure-based design of a fusion glycoprotein vaccine for respiratory syncytial virus. *Science* **342**, 592–598 (2013).
59. R. N. Kirchdoerfer, C. A. Cottrell, N. Wang, J. Pallesen, H. M. Yassine, H. L. Turner, K. S. Corbett, B. S. Graham, J. S. McLellan, A. B. Ward, Pre-fusion structure of a human coronavirus spike protein. *Nature* **531**, 118–121 (2016).
60. J. C. Milligan, C. W. Davis, X. Yu, P. A. Ilinykh, K. Huang, P. J. Halfmann, R. W. Cross, V. Borisevich, K. N. Agans, J. B. Geisbert, C. Chennareddy, A. J. Goff, A. E. Piper, S. Hui, K. C. L. Shaffer, T. Buck, M. L. Heinrich, L. M. Branco, I. Crozier, M. R. Holbrook, J. H. Kuhn, Y. Kawaoka, P. J. Glass, A. Bukreyev, T. W. Geisbert, G. Worwa, R. Ahmed, E. O. Saphire, Asymmetric and non-stoichiometric glycoprotein recognition by two distinct antibodies results in broad protection against ebolaviruses. *Cell* **185**, 995–1007.e18 (2022).
61. J. Gorman, G.-Y. Chuang, Y.-T. Lai, C.-H. Shen, J. C. Boyington, A. Druz, H. Geng, M. K. Louder, K. M. Kee, R. Rawi, R. Verardi, Y. Yang, B. Zhang, N. A. Doria-Rose, B. Lin, P. L. Moore, L. Morris, L. Shapiro, J. R. Mascola, P. D. Kwong, Structure of super-potent antibody CAP256-VRC26.25 in complex with HIV-1 envelope reveals a combined mode of trimer-apex recognition. *Cell Rep.* **31**, 107488 (2020).
62. J. H. Lee, R. Andrabi, C. Y. Su, A. Yasmeen, J.-P. Julien, L. Kong, N. C. Wu, R. McBride, D. Sok, M. Pauthner, C. A. Cottrell, T. Nieusma, C. Blattner, J. C. Paulson, P. J. Klasse, I. A. Wilson, D. R. Burton, A. B. Ward, A broadly neutralizing antibody targets the dynamic HIV envelope trimer apex via a long, rigidified, and anionic β-hairpin structure. *Immunity* **46**, 690–702 (2017).
63. Q. Liu, P. Acharya, M. A. Dolan, P. Zhang, C. Guzzo, J. Lu, A. Kwon, D. Gururani, H. Miao, T. Bylund, G.-Y. Chuang, A. Druz, T. Zhou, W. J. Rice, C. Wigge, B. Carragher, C. S. Potter, P. D. Kwong, P. Lusso, Quaternary contact in the initial interaction of CD4 with the HIV-1 envelope trimer. *Nat. Struct. Mol. Biol.* **24**, 370–378 (2017).
64. J. S. McLellan, M. Chen, S. Leung, K. W. Graepel, X. du, Y. Yang, T. Zhou, U. Baxa, E. Yasuda, T. Beaumont, A. Kumar, K. Modjarrad, Z. Zheng, M. Zhao, N. Xia, P. D. Kwong, B. S. Graham, Structure of RSV fusion glycoprotein trimer bound to a prefusion-specific neutralizing antibody. *Science* **340**, 1113–1117 (2013).
65. D. Tian, M. B. Battles, S. M. Moin, M. Chen, K. Modjarrad, A. Kumar, M. Kanekiyo, K. W. Graepel, N. M. Taher, A. L. Hotard, M. L. Moore, M. Zhao, Z.-Z. Zheng, N.-S. Xia, J. S. McLellan, B. S. Graham, Structural basis of respiratory syncytial virus subtype-dependent neutralization by an antibody targeting the fusion glycoprotein. *Nat. Commun.* **8**, 1877 (2017).
66. Z. Wang, M. Amaya, A. Addetia, H. V. Dang, G. Reggiano, L. Yan, A. C. Hickey, F. DiMaio, C. C. Broder, D. Veesler, Architecture and antigenicity of the Nipah virus attachment glycoprotein. *Science* **375**, 1373–1378 (2022).
67. A. Talekar, I. De Vito, Z. Salah, S. G. Palmer, A. Chattopadhyay, J. K. Rose, R. Xu, I. A. Wilson, A. Moscona, M. Porotto, Identification of a region in the stalk domain of the nipah virus receptor binding protein that is critical for fusion activation. *J. Virol.* **87**, 10980–10996 (2013).
68. M. A. Brindley, R. Suter, I. Schestak, G. Kiss, E. R. Wright, R. K. Plemper, A stabilized headless measles virus attachment protein stalk efficiently triggers membrane fusion. *J. Virol.* **87**, 11693–11703 (2013).
69. A. Talekar, A. Moscona, M. Porotto, Measles virus fusion machinery activated by sialic acid binding globular domain. *J. Virol.* **87**, 13619–13627 (2013).
70. E. M. Jurgens, C. Mathieu, L. M. Palermo, D. Hardie, B. Horvat, A. Moscona, M. Porotto, Measles fusion machinery is dysregulated in neuropathogenic variants. *MBio* **6**, e02528–e02514 (2015).
71. A. L. Greninger, D. M. Zerr, X. Qin, A. L. Adler, R. Sampoleo, J. M. Kuypers, J. A. Englund, K. R. Jerome, Rapid metagenomic next-generation sequencing during an investigation of hospital-acquired human parainfluenza virus 3 infections. *J. Clin. Microbiol.* **55**, 177–182 (2017).
72. D. N. Mastronarde, Automated electron microscope tomography using robust prediction of specimen movements. *J. Struct. Biol.* **152**, 36–51 (2005).
73. D. N. Mastronarde, S. R. Held, Automated tilt series alignment and tomographic reconstruction in IMOD. *J. Struct. Biol.* **197**, 102–113 (2017).
74. D. Castaño-Díez, M. Kudryashev, H. Stahlberg, Dynamo Catalogue: Geometrical tools and data management for particle picking in subtomogram averaging of cryo-electron tomograms. *J. Struct. Biol.* **197**, 135–144 (2017).
75. S. H. W. Scheres, RELION: Implementation of a Bayesian approach to cryo-EM structure determination. *J. Struct. Biol.* **180**, 519–530 (2012).
76. Y. Z. Tan, P. R. Baldwin, J. H. Davis, J. R. Williamson, C. S. Potter, B. Carragher, D. Lyumkis, Addressing preferred specimen orientation in single-particle cryo-EM through tilting. *Nat. Methods* **14**, 793–796 (2017).
77. E. F. Pettersen, T. D. Goddard, C. C. Huang, G. S. Couch, D. M. Greenblatt, E. C. Meng, T. E. Ferrin, UCSF Chimera—A visualization system for exploratory research and analysis. *J. Comput. Chem.* **25**, 1605–1612 (2004).
78. J. R. Kremer, D. N. Mastronarde, J. R. McIntosh, Computer visualization of three-dimensional image data using IMOD. *J. Struct. Biol.* **116**, 71–76 (1996).
79. E. F. Pettersen, T. D. Goddard, C. C. Huang, E. C. Meng, G. S. Couch, T. I. Croll, J. H. Morris, T. E. Ferrin, UCSF ChimeraX: Structure visualization for researchers, educators, and developers. *Protein Sci.* **30**, 70–82 (2021).
80. P. V. Afonine, B. P. Klaholz, N. W. Moriarty, B. K. Poon, O. V. Sobolev, T. C. Terwilliger, P. D. Adams, A. Urzhumtsev, New tools for the analysis and validation of cryo-EM maps and atomic models. *Acta Crystallogr. D Struct. Biol.* **74**, 814–840 (2018).
81. A. Kucukelbir, F. J. Sigworth, H. D. Tagare, Quantifying the local resolution of cryo-EM density maps. *Nat. Methods* **11**, 63–65 (2014).
82. L. Zhang, A. Bukreyev, C. I. Thompson, B. Watson, M. E. Peeples, P. L. Collins, R. J. Pickles, Infection of ciliated cells by human parainfluenza virus type 3 in an in vitro model of human airway epithelium. *J. Virol.* **79**, 1113–1124 (2005).
83. A. M. Bolger, M. Lohse, B. Usadel, Trimmomatic: A flexible trimmer for Illumina sequence data. *Bioinformatics* **30**, 2114–2120 (2014).
84. P. Danecek, J. K. Bonfield, J. Liddle, J. Marshall, V. Ohan, M. O. Pollard, A. Whitwham, T. Keane, S. A. McCarthy, R. M. Davies, H. Li, Twelve years of SAMtools and BCFtools. *Gigascience* **10**, giab008 (2021).
85. D. C. Koboldt, Q. Zhang, D. E. Larson, D. Shen, M. D. McLellan, L. Lin, C. A. Miller, E. R. Mardis, L. Ding, R. K. Wilson, VarScan 2: Somatic mutation and copy number alteration discovery in cancer by exome sequencing. *Genome Res.* **22**, 568–576 (2012).

Acknowledgments: We thank the Imaging Suite at CUNY Advanced Science Research Center for instrument use. **Funding:** This work was supported by funding from the National Institutes of Health (AI152275 to T.C.M., AI121349 and AI160953 to M.P., GM133598 to A.d.G., and AI114736 and AI160961 to A.M.) and the Sharon Golub Fund at Columbia University Vagelos College of Physicians and Surgeons. **Author contributions:** Conceptualization: T.C.M., M.P., and A.M. Formal analysis: T.C.M., M.P., A.d.G., and A.M. Funding acquisition: T.C.M., M.P., A.d.G., and A.M. Investigation: T.C.M., G.Z., W.C., F.B., K.S., S.S., K.G., F.C., and D.P. Resources: A.L.G., A.d.G., M.P., and A.M. Supervision: T.C.M., A.L.G., M.P., A.d.G., and A.M. Writing (original draft): T.C.M. and A.M. Final version: All coauthors provided feedback to the final draft. **Competing interests:** The authors declare that they have no competing interests. **Data and materials availability:** All data needed to evaluate the conclusions in the paper are present in the paper and/or the Supplementary Materials. Final subtomogram averages have been deposited in the Electron Microscopy Data Bank (EMDB) with the accession codes EMD-27550 for the HN and F complex

and EMD-27551 for the PIA174 antibody and F complex. Prealigned tilts for all tomograms have been deposited in the Electron Microscopy Public Image Archive (EMPIAR) database with the accession codes EMPIAR-11103 for the HN and F complex and EMPIAR-11104 for the PIA174 antibody and F complex. The reagents can be provided by the corresponding authors' pending scientific review and a completed material transfer agreement. Requests for the reagents should be submitted to am939@cumc.columbia.edu.

Submitted 4 August 2022
Accepted 6 January 2023
Published 10 February 2023
10.1126/sciadv.ade2727